Near-native state imaging by cryo-soft-X-ray tomography reveals remodelling of multiple cellular organelles during HSV-1 infection

Kamal L. Nahas[1,3], Viv Connor[1], Katharina M. Scherer[2], Clemens F. Kaminski[2], Maria Harkiolaki[3]*, Colin M. Crump[1]*, Stephen C. Graham[1]*

[1]Department of Pathology, University of Cambridge, Cambridge, United Kingdom.

[2]Department of Chemical Engineering and Biotechnology, University of Cambridge, Cambridge, United Kingdom.

[3]Beamline B24, Diamond Light Source, Didcot, United Kingdom.

*Corresponding authors: maria.harkiolaki@diamond.ac.uk (MH); cmc56@cam.ac.uk (CMC); scg34@cam.ac.uk (SCG)

ORCIDs: KLN 0000-0003-3501-8473; KMS 0000-0002-2042-5407; CFK 0000-0002-5194-0962; MH 0000-0001-8091-9057; CMC 0000-0001-9918-9998; SCG 0000-0003-4547-4034

Contributions: Conceptualization: MH, CMC, SCG; Data Curation: KLN; Funding Acquisition: MH, CMC, SCG; Investigation: KLN, VC, KMS, CMC, SCG; Project Administration: MH, CMC, SCG; Resources: CFK, MH; Software: KLN; Supervision: MH, CMC, SCG; Visualization: KLN; Writing – Original Draft Preparation: KLN, CMC, SCG; Writing – Review & Editing: KLN, MH, CMC, SCG

Short Title: Cryo-soft-X-ray tomography of HSV-1 infection

Keywords: Herpesvirus, virus:host interactions, cryoSXT

Abstract

Herpes simplex virus-1 (HSV-1) is a large, enveloped DNA virus and its assembly in the cell is a complex multi-step process during which viral particles interact with numerous cellular compartments such as the nucleus and organelles of the secretory pathway. Transmission electron microscopy and fluorescence microscopy are commonly used to study HSV-1 infection. However, 2D imaging limits our understanding of the 3D geometric changes to cellular compartments that accompany infection and sample processing can introduce morphological artefacts that complicate interpretation. In this study, we used soft X-ray tomography to observe differences in whole-cell architecture between HSV-1 infected and uninfected cells. To protect the near-native structure of cellular compartments we used a non-disruptive sample preparation technique involving rapid cryopreservation, and a fluorescent reporter virus was used to facilitate correlation of structural changes with the stage of infection in individual cells. We observed viral capsids and assembly intermediates interacting with nuclear and cytoplasmic membranes. Additionally, we observed differences in the morphology of specific organelles between uninfected and infected cells. The local concentration of cytoplasmic vesicles at the juxtanuclear compartment increased and their mean width decreased as infection proceeded, and lipid droplets transiently increased in size. Furthermore, mitochondria in infected cells were elongated and highly branched, suggesting that HSV-1 infection alters the dynamics of mitochondrial fission/fusion. Our results demonstrate that high-resolution 3D images of cellular compartments can be captured in a near-native state using soft X-ray tomography and have revealed that infection causes striking changes to the morphology of intracellular organelles.

Author summary

Ultrastructural changes to the morphology and organization of cellular compartments during herpes simplex virus-1 (HSV-1) infection have not previously been studied under near-physiological conditions. In this study, soft X-ray tomography was used to image the ultrastructure of vitrified cells during HSV-1 infection. This technique allows visualisation of cellular organelles and viral capsids in relatively thick samples that are prepared by plunge cryocooling, without the need for chemical fixation or staining. We identified striking changes to the abundance and organization of multiple cellular organelles. The concentration of vesicles in the juxtanuclear region increased with time post infection, which could represent an increasing supply of vesicles to support capsid envelopment, and there is a transient increase in the size of lipid droplets in infected cells. Furthermore, we show that mitochondria elongate and form highly-branched networks as infection progresses. These findings offer insight into stages of virion morphogenesis and the cellular response to infection, highlighting the utility of cryo-soft-X-ray tomography for monitoring the near-native state ultrastructure of infected cells.

56 **Introduction**

57 Herpes simplex virus-1 (HSV-1) is a large, enveloped DNA virus in the *Alphaherpesvirinae* subfamily
58 of *Herpesviridae* that establishes a persistent life-long latent infection in sensory and sympathetic
59 neurons, occasionally reactivating to cause lytic replication in oral or genital mucosal epithelial cells that
60 culminates in cold sores and genital herpes, respectively [1]. The production of viral particles during
61 lytic replication is a complex process involving multiple cellular compartments [2–6].

62 In the first step of virion morphogenesis, capsid assembly and genome packaging occur in the nucleus
63 [7]. Fully formed nucleocapsids must cross the nuclear envelope to migrate into the cytoplasm to
64 undergo the latter stages of virus assembly – a process that involves close interaction between
65 nucleocapsids and the membranes of the nuclear envelope. Unlike individual proteins, the
66 nucleocapsids are too large to pass through nuclear pores and must therefore first bud into the
67 perinuclear space through the inner-nuclear membrane, forming a perinuclear viral particle (primary
68 envelopment). The envelope of this particle subsequently fuses with the outer-nuclear membrane to
69 release the nucleocapsid into the cytoplasm (de-envelopment)[8–11]. Numerous copies of multiple (≥
70 23) nuclear and cytoplasmic viral proteins deposit on their surface of nucleocapsids, forming the
71 amorphous proteinaceous layer known as the tegument [12]. Tegument proteins have multiple
72 important roles during infection, including the promotion of virion maturation [2,3,6]. Several cytoplasmic
73 compartments are essential to virion morphogenesis: viral proteins are synthesized and modified in the
74 endoplasmic reticulum and Golgi complex and, in a process known as secondary envelopment,
75 nucleocapsids acquire their membrane envelope from cytoplasmic vesicles that are thought to be
76 derived from the *trans*-Golgi network and the endosomal system [2,3,13]. In addition to compartments
77 directly involved in virion assembly, the cytoskeleton and other cellular organelles, such as mitochondria
78 and lysosomes, can become remodelled in response to infection [14–16]. Understanding how the
79 morphology and organization of cellular compartments change during infection could illuminate their
80 involvement in virion morphogenesis and in the cellular response to HSV-1 infection.

81 Previous studies to characterize remodelling of cellular compartments have identified numerous
82 changes that accompany HSV-1 infection, including the fragmentation of the Golgi complex and the
83 condensation of the endoplasmic reticulum around the nuclear rim [17,18]. A more comprehensive
84 study has recently been carried out using a recombinant form of HSV-1, known as the “timestamp”

85 reporter virus, expressing fluorescent chimeras of the early protein ICP0 and the late protein gC to
86 distinguish between early and late stages of infection [16]. Eight cellular compartments were compared
87 between uninfected and timestamp virus-infected human TERT-immortalized human foreskin fibroblast
88 (HFF-hTERT) cells, with high-resolution spatial data collected using structured illumination microscopy
89 (SIM) and expansion microscopy. Numerous changes in the morphology of cellular compartments were
90 observed as infection progressed, such as fragmentation of the Golgi complex at late stages of infection,
91 concentration of endosomes and lysosomes at a juxtanuclear compartment, and elongation of
92 mitochondria [16]. Mitochondrial morphology is known to vary in response to cellular energy demand,
93 oxidative stress, virus infection, and other stimuli [19–24]. For example, varying energy demand within
94 a cell affects mitochondrial length in order to tune the level of ATP production, and fusion of normal and
95 damaged mitochondria during high oxidative stress dilutes the impact of reactive oxygen species on
96 mitochondrial function [19,20,24]. Furthermore, mitochondria associate with the cellular microtubule
97 network, which is known to be altered via breakdown and dispersal of the microtubule organising centre
98 during HSV-1 infection [25]. Deregulation of microtubule dynamics may also affect the organisation of
99 cytoplasmic vesicles and their migration from the perinuclear region towards the cell surface.

100 The extent to which sample preparation strategies alter the morphology of cellular structures remains
101 poorly understood and it is possible that disruptive techniques such as immunostaining or sample
102 expansion could introduce artefacts in cellular ultrastructure [26–28]. Moreover, it is not clear if the
103 changes to cellular compartments that have been observed previously are consistent across different
104 cell types used to study HSV-1 infection. Soft X-ray tomography of cryopreserved samples (cryoSXT)
105 offers an attractive alternative for the imaging of biological samples in a near-native state. Soft X-rays
106 used for cryoSXT have a lower energy (~500 eV)[29] and longer wavelength than the “hard” X-rays
107 typically used for medical imaging (~15–30 keV)[30] or X-ray crystallography (~6–20 keV)[31]. The
108 wavelengths of soft X-rays used for cryoSXT are in the “water window” where carbon-rich structures in
109 the cell such as membranes produce considerable contrast whereas oxygen-rich structures such as
110 the “watery” cytosol remain transparent, thereby enabling cellular compartments to be observed [29].
111 This label-free technique can be used to image the ultrastructure of infected (and control) cells,
112 monitoring the 3D geometry and organization of cellular compartments [32]. Furthermore, by using non-
113 disruptive cryopreservation protocols, such as plunge cryocooling in the case of cryoSXT, the
114 ultrastructure of samples can be preserved in a near-native state for imaging [33]. CryoSXT is

115 particularly suitable for monitoring mitochondria because these cellular compartments produce a lot of
116 contrast owing to their carbon-rich cristae and matrix proteins [29].

117 In this study we applied cryoSXT to the study of ultrastructural changes that accompany HSV-1 infection
118 of human osteosarcoma U2OS cells, allowing comparison with previous fluorescence microscopy
119 investigations of HSV-1–infected HFF-hTERT cells [16]. The stage of HSV-1 infection in each individual
120 cell subjected to cryoSXT interrogation was determined by use of the timestamp HSV-1 reporter virus
121 and fluorescence cryo-microscopy. Although a few differences were observed between the extent of
122 Golgi fragmentation and the subcellular distribution of ICP0, we determined that remodelling of
123 cytoplasmic vesicles and mitochondria during infection was largely similar between these cultured cells.
124 Furthermore, the high resolution afforded by cryoSXT revealed that mitochondria become highly
125 branched during HSV-1 infection and that lipid droplets are enlarged at early times post-infection.

126 **Results**

127 *HSV-1 viral particles and assembly intermediates are detectable by cryoSXT*

128 Transmission electron microscopy (TEM) has been used extensively to visualise HSV-1 capsids in
129 infected cells [34–36]. However, TEM and cryoSXT have different strategies for introducing contrast in
130 imaging. In TEM, signal is produced by adding a contrast agent, whereas cryoSXT is label-free and
131 contrast is generated via the differential local density of carbon and oxygen in the material. Although
132 cryoSXT has been used previously to image virus particles in infected cells, it was unclear whether
133 individual 'naked' HSV-1 capsids, which are approximately 125 nm in diameter [32,37–40], would be
134 large enough and offer sufficient contrast to be observed with this imaging method. To establish a
135 baseline, we grew uninfected HFF-hTERT cells on perforated carbon electron microscopy (EM) grids
136 and plunge cryocooled them for imaging by cryoSXT. Unlike a glass lens that focuses light by refraction,
137 a zone plate was used to focus the X-rays by diffraction: a zone plate is a diffraction grating composed
138 of a series of concentric rings in which alternating rings are transparent to X-rays and the resolution is
139 determined by the diameter of the outermost ring [41]. An objective zone plate with 25 nm outer zone
140 was used for our experiments here, affording image resolution of up to 30 nm. To produce a 3D imaging
141 volume (tomogram), a series of X-ray projection images (tilt series) were collected from a single
142 9.46×9.46 µm field of view in the cell, with each projection collected following rotation of the specimen
143 around an axis normal to the incident X-ray beam. For each tomogram the projections spanned up to
144 120° of rotation with increments of 0.2° or 0.5° per image. To correct for small inaccuracies in the tilting
145 of the microscope stage during imaging, the projections in the series were aligned together in the
146 program IMOD [42] using gold fiducials or lipid droplets as landmarks for registration. We collected 19
147 tilt series that were processed into 3D tomograms. We found that uninfected cell nuclei lacked distinctive
148 internal features other than a difference in average intensity when compared with the cytosol (**Fig 1A**).

149 Given that the nucleus is the site of capsid assembly, we sought to determine whether an abundance
150 of capsids could be detected in infected cells. To this end, HFF-hTERT cells were cultured on
151 perforated-carbon EM grids, infected with HSV-1 at a multiplicity of infection (MOI) of 2 and plunge
152 cryocooled at 16 hours post-infection (hpi). Infected cells were imaged via cryoSXT using a 40 nm zone
153 plate objective, illuminating a 15.14×15.14 µm field of view, using the image acquisition and analysis
154 workflow detailed above (**Fig. 1B**). These samples were prepared and cryopreserved on three separate

155 occasions and 98 tomograms were collected in total. Numerous dark puncta were observed in the
156 nucleus of infected cells (**Fig. 1C**). We interpreted these puncta to be HSV-1 capsids because capsids
157 are rich in carbon and phosphorous, being proteinaceous shells surrounding tightly packed DNA
158 genomes, and these elements exhibit strong absorption at the 500 eV X-ray energy used here for
159 imaging [29].

160 During virus assembly, capsids enter the perinuclear space by budding at the inner nuclear membrane
161 (primary envelopment), forming a membrane-wrapped perinuclear virus particle that rapidly fuses with
162 the outer nuclear membrane *en route* to the cytoplasm [11]. These enveloped virions in the perinuclear
163 space are infrequently observed by EM [5,43–46] because they are short-lived and the thin sectioning
164 required for imaging using electrons decreases the probability that such structures will be present within
165 the cellular volume being examined. The penetrating power of soft X-rays in unstained cryopreserved
166 samples (> 10 μm in depth) removes the requirement for sectioning, allowing the entire depth of the
167 cell to be imaged for any given field of view. This increases the likelihood of observing short-lived
168 structures such as primary enveloped virus particles. Dark puncta within the nuclear envelope that are
169 likely to be perinuclear viral particles were found 11 times in 98 tomograms (**Fig. 1D**). The perinuclear
170 viral particles appear to expand the perinuclear space and the nuclear envelope, as shown in a
171 segmented image (**Fig. 1E**). The width of the nuclear envelope at putative sites of primary envelopment
172 (190.5 ± 6.01 nm SEM; N=11) is significantly greater than the width of the nuclear envelope in other
173 places on the same tomograms (99.8 ± 3.57 nm SEM; N=11; paired t-test p-value=1.93×10^{-9}) (**Fig. 1F**).
174 This demonstrates that substantial deformation of the nuclear envelope must occur to accommodate
175 the presence of perinuclear virus particles.

176 Dark puncta representing viral capsids were also observed in the cytoplasm in close proximity to
177 vesicles, highlighting potential sites of secondary envelopment (**Fig. 1G**). After secretion, HSV-1
178 particles commonly remain bound to the cell surface, a property that may be exacerbated by the antiviral
179 restriction factor tetherin [47,48]. In addition, we expected to see HSV-1 particles between cells because
180 virions are targeted to cell junctions to promote cell-cell spread [49]. Linear arrays of dark puncta were
181 observed on the cell surface and between cells (**Fig. 1H and 1I**) and likely represent released virus
182 particles (extracellular virions). Virus particles increase in size during the assembly process as they
183 accumulate their tegument and become enveloped in the cytoplasm before they are released from the

184 cell. We measured the width of nuclear capsids and extracellular virions from 8 tomograms to determine
185 if they could be distinguished based on their size (**Fig. 1J**). Nuclear capsids had a width of 125.8 ± 1.70
186 nm SEM (n=80 from 4 tomograms; range 96–160 nm; SD 15.22 nm), which is consistent with high-
187 resolution structural analysis of purified capsids (~125 nm)[38] and of capsids inside infected-cell nuclei
188 [50]. Extracellular virions were larger with a width of 198.6 ± 3.48 nm SEM (n=80 from 4 tomograms;
189 range 128–272 nm; SD 31.15 nm), consistent with previous reports (~175-200 nm) [37,51]. These
190 differences were found to be significant with a Mann-Whitney *U* test for unequal variance (W=126, *p*-
191 value$<2.2\times10^{-16}$).

192 *Fluorescently tagged ICP0 and gC can be used to monitor the progression of HSV-1 infection in HFF-*
193 *hTERT and U2OS cells*

194 Recent microscopy and single-cell transcriptomics studies have revealed that, even in a monolayer of
195 cultured cells synchronously infected with HSV-1, individual cells progress through the infection cycle
196 at different rates and the remodelling of cellular compartments varies depending on the stage of
197 infection [16,52]. To control for this, a recombinant strain of HSV-1 termed the timestamp virus has
198 been developed to allow identification of the stage of infection based on the abundance and subcellular
199 localization of the fluorescently tagged early and late viral proteins ICP0 and gC, respectively [16].
200 Fluorescence microscopy of HFF-hTERT cells infected with this timestamp virus allowed
201 characterization of the changes to cellular compartments that accompany progressing HSV-1 infection
202 and categorization of cells into 4 stages of infection. Having confirmed that virus particles could be
203 observed in infected cells using cryoSXT, we sought to obtain higher-resolution temporal information
204 on the morphological changes that occur over the course of HSV-1 infection by using the timestamp
205 virus. Preliminary experiments performed using infected HFF-hTERT cells were unsuccessful as they
206 proved sensitive to prolonged exposure to the soft X-ray beam when collecting data with a 25 nm zone
207 plate, the objective available at the time on the microscope at the synchrotron beamline used for these
208 experiments, leading to localized sample heating and low-quality tomograms. We thus turned instead
209 to U2OS osteosarcoma cells, which have been used previously for HSV-1 ultrastructural analysis
210 [53,54] and have been shown previously to be robust imaging subjects that yield consistently high-
211 quality tomograms when exposed to high doses of soft X-rays [32,33].

212 To compare the temporal profiles of progression of timestamp HSV-1 infection in HFF-hTERT and
213 U2OS cells, we first compared the expression patterns of the fluorescently tagged proteins between
214 the two cell types. Cells were infected at an MOI of 1–3 and samples were fixed at multiple time points
215 following infection before imaging on a widefield fluorescence microscope (**Fig. 2**). The immediate-early
216 HSV-1 protein ICP0 was used to characterize early stages of infection because it is one of the first viral
217 proteins to be expressed [55]. In both cell lines, eYFP-ICP0 was expressed throughout the course of
218 infection. However, the spatial localization of eYFP-ICP0 differed somewhat between HFF-hTERT and
219 U2OS cells. In HFF-hTERT cells, eYFP-ICP0 was observed in the nucleus in stage 1 whereas it became
220 more concentrated in the cytoplasm with relatively weaker signal in the nucleus in stages 2–4. However,
221 in U2OS cells, eYFP-ICP0 expression displayed a high signal in the nucleus throughout infection while
222 also becoming more concentrated in the cytoplasm as infection progressed, suggesting U2OS cells
223 retain more eYFP-ICP0 in the nucleus at the later stages of infection than is observed for HFF-hTERT
224 cells (**Fig. 2A**). This may reflect differences in cellular interactions for ICP0 in U2OS cells, which is
225 consistent with previous observations demonstrating that replication deficits demonstrated by ICP0-null
226 strains of HSV-1 in human fibroblasts are effectively complemented in U2OS cells [56]. The continued
227 high signal levels of eYFP-ICP0 in the nucleus complicated the distinction between the early stages
228 (stages 1+2) of infection in U2OS cells.

229 The spatial expression of gC-mCherry was broadly similar between HFF-hTERT and U2OS cells. gC
230 is a viral glycoprotein expressed at late stages of virus replication [57] that is incorporated into nascent
231 virus particles at sites of virus envelopment [58]. In HFF-hTERT cells, gC-mCherry was enriched at a
232 juxtanuclear site in stage 3 but became fragmented and dispersed throughout the cytoplasm and at the
233 plasma membrane by stage 4 (**Fig. 2A**). A similar spatial expression was observed for late stage U2OS
234 cells, with redistribution of gC from juxtanuclear sites to the periphery likely representing progressively
235 later stages of infection. However, there existed a continuum of gC distribution between juxtanuclear
236 and dispersed in late stages of infection in U2OS cells. This, combined with the difficulties in
237 differentiating between early infection stages due to nuclear retention of eYFP-ICP0, led us to group
238 U2OS infection stages into two broader categories (“early” and “late”). The designation of early or late-
239 stage infection was determined by the absence or presence of gC-mCherry signal in eYFP-ICP0
240 positive cells, respectively.

241 Next, we probed whether progression through the replication cycle follows the same timecourse in HFF-
242 hTERT and U2OS cells. Both cell types were inoculated with timestamp virus (MOI 3) for one hour, at
243 which time unabsorbed viruses were inactivated with a citric acid wash, and cells were fixed at various
244 time points over the course of 24 hrs before imaging (**Fig. 2B**). We observed that the infection proceeds
245 at a similar pace in both cells types, with a similar proportion of cells in equivalent stages of infection
246 (1+2/early and 3+4/late) at each time point.

247 *CryoSXT following infection with 'timestamp' HSV-1 allows temporal correlation of ultrastructural*
248 *changes during infection*

249 To characterize the changes in morphology of cellular compartments that accompany different stages
250 of virus infection, U2OS cells were grown on perforated-carbon EM grids before being infected (or mock
251 infected) with timestamp HSV-1 and cryogenically preserved by plunge cryocooling in liquid nitrogen-
252 cooled liquid ethane (**Fig. 3A**). Vitrified samples were analysed by cryo-widefield microscopy to classify
253 the stage of infection and then imaged using cryoSXT to correlate the stage of virus infection in a
254 specific cell with observed morphological changes (**Fig. 3B**). Cells were infected at MOI 1 and the
255 samples were plunge cryocooled at 9 hpi in an attempt to evenly sample the different stages of infection
256 (**Fig. 2B**). In total, 139 tomograms were reconstructed; 76 from uninfected cells alongside 22 and 41
257 from cells at early or late stages of infection, respectively, across three independent replicates (**Table**
258 **1**). Manual inspection of the resultant tomograms revealed that the 25 nm zone plate allows detection
259 of higher resolution features than is possible with the 40 nm zone plate, such as the lumen of the
260 endoplasmic reticulum, cytoskeletal filaments, and small membrane structures (**S1A-E Figs**). The
261 observed width of nuclear capsids in U2OS cells imaged using the 25 nm zone plate (**S1F Fig**) is similar
262 to those observed in infected HFF-hTERT cells imaged using the 40 nm zone plate (**Fig. 1J**). The
263 tomograms collected from U2OS cells using the 25 nm zone plate were thus deemed suitable for
264 identifying changes to cellular compartments that occur during HSV-1 infection.

265 We observed that HSV-1 infection does not dramatically affect the morphology of the nucleus or integrity
266 of the nuclear envelope, despite the continuous budding and fusion of capsids that occur at the inner
267 and outer nuclear membranes, respectively, during infection. We occasionally observed bulging of the
268 nuclear envelope into the cytoplasm without separation of the inner and outer nuclear membranes (**S1G**
269 **Fig**). This bulging could be seen in both uninfected and infected cells. It was distinct from the separation

270 of the inner and outer nuclear membranes caused by the expansion of the perinuclear space, which we
271 observed in the presence of perinuclear viral particles (**Fig. 1D–F**). It also differed from the expansion
272 of the perinuclear space observed previously in uninfected murine adenocarcinoma cells imaged using
273 cryoSXT [59]. The cryopreservation protocol used for preparing our cryoSXT samples does not result
274 in dehydration artefacts that can alter the apparent morphology of the nuclear membrane in TEM
275 samples [59], suggesting that these bulges are not artefacts of the sample preparation, but the biological
276 relevance of this observation remains unclear.

277 Striking changes were observed in the size and dispersal of vesicles during HSV-1 infection (**Fig. 4A**
278 and **S1 Video**). HSV-1 capsids are thought to interact with several types of vesicles in the cytoplasm,
279 including *trans*-Golgi network vesicles and endosomes, both of which have been implicated in
280 secondary envelopment [13]. Infected cells had a greater number of vesicles in juxtanuclear regions
281 when compared with uninfected cells (**Fig. 4A and S2 Video**). To determine if there was a difference
282 in the size of vesicles between uninfected cells and those at early- or late-stages of infection we
283 developed *Contour*, a program to segment and quantitate cellular features in 3D volumes [60]. The
284 widest point of each vesicle in three dimensions from 4 tomograms for each condition was measured
285 (**Fig. 4B**). The mean vesicle width was higher for uninfected cells (802.23 ± 348.47 nm SD, N=96) than
286 for early-stage (688.66 ± 271.76 nm SD, N=184) and late-stage (631.85 ± 270.60 nm SD, N=184)
287 infected cells. The mean vesicle widths for each tomogram were compared using a one-way ANOVA
288 and Tukey test and the vesicle widths of uninfected cells were found to be significantly different from
289 early-stage ($p=0.04$) and late-stage ($p=0.01$) infected cells. The vesicle width did not differ significantly
290 between early-stage and late-stage infected cells ($p=0.62$). Segmented vesicles (**Fig. 4A**) were open-
291 ended because the contrast of membranes in the sample differs based on their orientation with respect
292 to incident X-ray beam. This arises because the sample can only be rotated by 120° during cryoSXT tilt
293 series image acquisition, rather than 180° as would be required for isotropic data collection, due to
294 geometric constraints between microscope and sample holder components. The edges of vesicles that
295 lie parallel to the incident X-ray beam (i.e. the 'sides' of the vesicle with respect to the XY projection
296 plane) produce high contrast, since the X-rays pass tangentially through the carbon-rich membrane of
297 the vesicle and thus traverse a large volume of material that strongly absorbs X-rays. The 'front' and
298 'back' edges of the vesicle with respect to the XY projection plane yield less contrast because the X-
299 rays pass radially through these membranes, traversing a shorter path through this carbon-rich X-ray

300 absorbing material. The lower contrast for the front and back edges of vesicles prevented their reliable
301 segmentation, yielding gaps in the resultant volumes.

302 Lipid droplets are carbon-dense organelles that produce high contrast in cryoSXT and were clearly
303 visible as dark solid spheres in the tomograms. These lipid droplets could be readily segmented using
304 *Contour* [60], allowing measurement of their volumes. We observed an increase in the volume of these
305 droplets in cells during the early stage of infection when compared with uninfected cells or to cells at
306 the late stage of infection (**Fig. 4C**). A small number of extremely large lipid droplets ($>5\times10^7$ nm^3) were
307 observed in tomograms from each of the three replicate infections, but the presence of these large
308 droplets was not correlated with progression through the infection (**S2A-B Figs**). The distribution of lipid
309 droplet sizes was non-Gaussian (positively skewed; **S2C Fig**) and a non-parametric Mann-Whitney *U*
310 test confirmed that, in all three replicate experiments, the lipid droplets were significantly larger in cells
311 at early stages of infection than in uninfected cells (**S2D Fig**). There is not a consistent difference in the
312 size of lipid droplets between uninfected cells and those at late stages of infection, suggesting that lipid
313 droplets undergo a transient change in size during infection.

314 Mitochondria were the most phenotypically diverse organelles monitored in this study. In most cases,
315 they were thin and possessed a dark matrix (**Fig. 5A**). However, occasionally there were cells that
316 contained swollen mitochondria with a lighter matrix with highly contrasting cristae (**S3A Fig**), similar to
317 observations of mitochondria made by EM [61–63] and cryoSXT [59]. This swollen morphology can be
318 associated with release of cytochrome *c* from porous mitochondria during apoptosis [61]. Swollen
319 mitochondria were observed in each of the three independent sets of cell growth, infection and plunge
320 cryocooling experiments performed, but these swollen mitochondria were most prevalent in the
321 uninfected cells of replicate 3 (**S3B Fig**). In uninfected cells, non-swollen mitochondria were
322 heterogeneous in shape, with numerous being small and spherical or long and curved in the same cell
323 (**Fig. 5A**). We observed branching in some elongated mitochondria. However, mitochondria appeared
324 less heterogenous in shape in infected cells, and were consistently more elongated and branched (**Fig.
325 5B-D, S3C Fig,** and **S3 Video**), in line with previous observations made using super-resolution
326 fluorescence microscopy of HFF-hTERT cells infected with the timestamp virus [16]. The number of
327 points where mitochondria branch into two or more arms (branching nodes) was significantly increased
328 ($p<0.05$) in cells at late stages of infection (20.5 ± 5.45 nodes SD; n = 15) compared with uninfected

329 cells (7.0 ± 4.02 nodes SD; n = 15) according to a one-way ANOVA and Tukey tests performed on each
330 replicate (**Fig. 5D**). In some cases, the mitochondria fused into a single, branched network (**Fig. 5B** and
331 **S3 Video**), providing a dramatic demonstration of the increase in mitochondrial branching and decrease
332 in number of distinct mitochondrial networks that accompanies HSV-1 infection. It was also observed
333 that the number of distinct mitochondria decreased in infected cells, although ambiguity regarding the
334 connectivity of mitochondrial networks that extend beyond the tomogram field-of-view prevented
335 precise quantitation of this effect. Confocal microscopy qualitatively confirmed the observations made
336 with cryoSXT that mitochondria appear more elongated in infected cells and that mitochondrial
337 morphology in peripheral areas of the cell was more heterogenous in uninfected cells than in infected
338 cells (**S4 Fig.**). However, the limited resolution of confocal imaging made it difficult to differentiate
339 between highly-branched and separate-but-overlapping mitochondria, particularly at crowded
340 juxtanuclear locations.

341 *Golgi membranes and the microtubule network are disrupted during HSV-1 infection of U2OS cells*

342 HSV-1 infection is known to be accompanied by dispersal of the Golgi complex and fragmentation of
343 the *trans*-Golgi network [16,64,65]. However, Golgi-related compartments can be difficult to distinguish
344 from other vesicular compartments by cryoSXT and are infrequently observed [59]. We therefore used
345 SIM super-resolution fluorescence microscopy to monitor the changes in Golgi organisation that
346 accompany HSV-1 infection. Fixed U2OS cells that had been infected (MOI 3) with the timestamp
347 reporter HSV-1 for 6 hours were immunostained with the *cis*-Golgi marker GM130, demonstrating that
348 the GM130^{+} Golgi membranes are clustered with a tubular morphology at early stages of infection (**Fig.**
349 **6A**). In cells at late stages of infection the distribution of GM130 was more punctate and more widely
350 distributed throughout the cell, consistent with fragmentation of the Golgi (**Fig. 6B**). The gC-mCherry
351 signal was also present at multiple sites throughout the cell, often adjacent to the GM130 signal (**Fig.**
352 **6B**). SIM imaging of infected U2OS cells stained with the *trans*-Golgi network marker TGN46 also
353 demonstrated increasing dispersion of TGN46^{+} membranes at late- versus early-stages of infection
354 (**Fig. 7**) and again we observed that the TGN46 signal was adjacent to, or partially overlapping with,
355 gC-mCherry signal in cells at late stages of infection (**Fig. 7B**).

356 As demonstrated above, HSV-1 infection of U2OS cells changes the morphology of lipid droplets,
357 mitochondria, vesicles and Golgi membranes, all of which interact with the microtubule network [66–

358 69]. While cytoskeletal filaments can occasionally be observed using cryoSXT (**S1C Fig**), microtubules
359 are too thin (25 nm width)[70] to be reliably detected using this technique. We therefore used confocal
360 fluorescence microscopy to study microtubule morphology in uninfected U2OS cells or cells infected
361 with timestamp HSV-1 (MOI 3) at early and late stages of infection, captured at 6 and 16 hpi,
362 respectively. Microtubules were monitored by immunolabelling β-tubulin. In uninfected cells
363 microtubules formed long filaments that radiated out of a prominent microtubule organising centre
364 (MTOC) (**Fig. 8A**). By early stages of infection, MTOCs were less pronounced and microtubules no
365 longer had a well-dispersed, radial distribution (**Fig. 8B**). At late stages of infection, MTOCs could not
366 be detected in most cells, the microtubule network became more compact, and fewer long filaments
367 were observed (**Fig. 8C**).

368 **Discussion**

369 In this study, we demonstrated that cryoSXT can be used to monitor the production of nascent HSV-1
370 particles and observed changes to the architecture of cellular compartments during infection. The
371 sizeable field of view and penetrating power of X-rays facilitate cryoSXT imaging throughout the depth
372 of the cell, allowing rare or transient events to be captured such as the transit of nascent capsids through
373 the nuclear envelope. Furthermore, the lack of requirement for contrast-enhancing agents or chemical
374 fixation allows direct imaging of cellular compartments in a near-native state. We exploited these
375 properties of cryoSXT to compare the morphology of cellular compartments between uninfected and
376 infected U2OS cells, using a recombinant strain of HSV-1 expressing fluorescently tagged early and
377 late viral proteins to identify the infection stage of individual cells within the virus-inoculated samples.

378 CryoSXT has several advantages as a technique for probing the ultrastructure of cells, plus a number
379 of limitations. CryoSXT imaging is performed on samples that have been vitrified through plunge
380 cryocooling. This rapid and convenient sample preparation technique preserves cellular ultrastructure
381 in a near-native state, avoiding the artefacts that have been associated with chemical fixation,
382 dehydration, and resin-embedding for TEM analysis [29] and yielding higher label-free contrast than is
383 obtained using cryoET [71]. Furthermore, the penetrating power of X-rays means that samples up to
384 10 μm thick can be imaged by cryoSXT [29]. As the U2OS cells we investigated had an average depth
385 of approximately 3 μm, each X-ray tomogram contained hundreds of projections through the entire
386 depth of the cell. This contrasts with TEM, cryoEM, and cryoET imaging, which generally require ultra-
387 thin sectioning or focused ion beam (FIB)-milling of samples into ~0.5–1.0 μm lamella such that the
388 entire depth of an adherent cell like U2OS cannot be collected in one acquisition [72–74]. CryoSXT
389 images a large field of view (9.46×9.46 μm and 15.14×15.14 μm with the 25 nm and 40 nm zone plates,
390 respectively), allowing regions of the nucleus, perinuclear space, and peripheral cytoplasm to be
391 captured together. Lastly, cryoSXT is a relatively high-throughput imaging technique, with each
392 tomographic dataset taking only 5–20 minutes to collect depending on X-ray beam brightness, exposure
393 time, angular rotation per frame and total rotation range used for tomogram acquisition [29]. As we
394 demonstrated in this study, the ability to conveniently prepare samples and collect multiple tomograms
395 expands the number of cells that can be interrogated, allowing robust numerical analysis of the
396 biological specimen under investigation. For example, by using the semi-automated segmentation tool

397 *Contour* [60] we were able to analyse the volumes of 4845 individual lipid droplets, acquired across 94
398 tomograms from three biological replicate HSV-1 infections, unambiguously demonstrating a transient
399 increase in lipid droplet volume at the early stage of infection (**Fig. 4C**, **S2 Fig.**). We also demonstrate
400 that cryoSXT can be used to perform accurate quantitative analyses of geometric properties of the
401 samples. For example, our measurements of widths of capsids and extracellular virions, determined
402 from 80 observations of each from 4 individual tomograms, were consistent with measurements
403 obtained using cryoEM, cryoET, and dSTORM [37,38,51].

404 The main drawback of cryoSXT for the analysis of biological samples is the limited resolution of this
405 technique when compared with TEM, cryoEM or cryoET. Whereas TEM and cryoET can reach near-
406 atomic and atomic resolution, respectively [72,73], cryoSXT imaging of cells with a 25 nm zone plate
407 can only achieve an effective resolution of approximately 30 nm [32]. This allows imaging of cellular
408 compartments and virus particles, as we demonstrate in this study, but it does not allow the reliable
409 imaging of cytoskeletal components or of individual macromolecular complexes such as proteasomes
410 or ribosomes [75,76]. The zone plate installed on an X-ray microscope is often outside the control of
411 the end user, but our experience in this study was that use of the 25 nm zone plate did not provide
412 significant additional *biological* information when compared with data collected with the 40 nm zone
413 plate. An additional drawback of cryoSXT is that the relatively low resolution of the images can
414 complicate the differentiation of cellular membrane-bound structures such as autophagosomes,
415 vesicles and other organelles. However, this limitation can be addressed by correlative cryo-microscopy
416 of vitrified samples expressing fluorescent marker proteins, for example the fluorescently-tagged HSV-
417 1 envelope glycoprotein gC that was used in this study to identify sites of virus assembly. Extending
418 the resolution of correlative fluorescence cryo-microscopy using cryoSIM [32], or increasing the contrast
419 in cryoSXT of specific features in cells via live-cell labelling with metals [77], are promising future
420 avenues that will address some of the limitations of cryoSXT and extend its utility for biological imaging.

421 HFF-hTERT and U2OS cells are commonly used for the study of HSV-1 infection [16,53,54]. We had
422 originally intended to use only HFF-hTERT cells for this study, to allow comparison with super-resolution
423 fluorescence microscopy studies [16], but found infected HFF-hTERT cells to be less amenable to
424 interrogation by cryoSXT than other cell lines, such as U2OS cells. We therefore explored the
425 differences in the dynamics of viral infection between HFF-hTERT and U2OS cells using the timestamp

426 virus. In general, the modifications to cellular compartments observed in this study largely replicated
427 those observed in HFF-hTERT cells [16], suggesting the interactions between viral components and
428 cellular compartments are broadly similar in these two cell types. We observed subtle differences
429 between the infections in these cells, including a change in the nuclear-to-cytoplasmic translocation of
430 the early viral protein ICP0 (**Fig. 2**). Residues important for the nuclear import/export dynamics of ICP0
431 have previously been identified: ICP0 possesses a canonical nuclear localization signal at residues
432 500–506 and deletion of 57 residues from the C terminus abolishes nuclear export of ICP0 [78].
433 Although residues important for trafficking of ICP0 have been mapped, the cellular proteins involved in
434 ICP0 trafficking have yet to be identified. In this study, a higher intensity of eYFP-ICP0 was detected in
435 the nucleus compared with the cytoplasm of infected U2OS cells at every timepoint. In contrast, higher
436 cytoplasmic intensity of ICP0 is observed at late stages of infection in HFF-hTERT cells and other cell
437 lines [16,79,80]. This suggests that the expression of host proteins that regulate nuclear import and/or
438 export of ICP0 may differ in U2OS cells. Several host proteins are known to participate in the nuclear
439 trafficking of EP0, the pseudorabies virus orthologue of ICP0: Ran, Importin α1, α3, α7, β1, and
440 transportin-1 [81]. Future work is required to identify whether U2OS cells are depleted or enriched in
441 proteins involved in nuclear import/export of ICP0, which may illuminate the mechanisms regulating
442 subcellular localisation of this important viral E3 ligase during infection.

443 Compared with uninfected U2OS cells, infected cells had a greater local concentration of detectable
444 vesicles in the juxtanuclear space (**Fig. 4**), consistent with previous research into the distribution of
445 vesicles during HSV-1 infection [16]. For instance, early endosomes and lysosomes have been shown
446 to accumulate at the juxtanuclear region during HSV-1 infection of HFF-hTERT cells [16]. This
447 reorganization of vesicle distribution may be related to a change in microtubule dynamics during
448 infection. Previous studies of HFF and Vero cells have shown that γ-tubulin and pericentrin, which are
449 components of the MTOC, become dispersed during alphaherpesvirus infection, suggesting breakdown
450 of the MTOC [25]. Thereafter microtubules polymerize at multiple foci in the cytoplasm rather than at a
451 single site and the growth rate, length, and stability of nascent microtubules become reduced compared
452 with uninfected cells [25]. We observed a decrease in the abundance of long microtubule filaments and
453 a disappearance of the MTOC as the infection progressed in U2OS cells (**Fig. 8**), consistent with these
454 previous studies. As the morphology of microtubules changes, the transport of vesicles towards the cell

455 periphery may become obstructed. This may result in the accumulation of vesicles at juxtanuclear
456 regions and may partly explain the increased local concentration of vesicles we observed.

457 An additional source of new vesicles may arise from the fragmentation of the Golgi complex during
458 HSV-1 infection [64]. Most of the evidence for Golgi fragmentation is based on the dispersion of several
459 Golgi markers (β-COP, Giantin, GM130, 58K protein, and beta-1,4-galactosyltransferase 1) throughout
460 the cytoplasm during HSV-1 infection as assessed by fluorescence microscopy [16,17,64]. Golgi
461 fragmentation has been studied to a lesser extent by ultrathin section EM, revealing that cisternae
462 become swollen and separated during infection [17]. Golgi fragmentation is thought to be a
463 consequence of disrupted microtubule dynamics and can be induced by treatment with nocodazole, an
464 inhibitor of β-tubulin polymerization [64]. Although our results are consistent with these observations,
465 the lack of markers for different types of vesicles meant that we could not determine if the vesicles we
466 observed with cryoSXT were Golgi-derived, of endosomal origin, or were unrelated to these cellular
467 compartments. We observed a reduction in the mean size of vesicles as the infection progressed
468 (**Fig. 4B**), which could arise either from fragmentation of the Golgi complex into small vesicles or an
469 inability of small vesicles to be trafficked from the juxtanuclear region to their target organelles via
470 microtubule transport. Furthermore, using SIM super-resolution fluorescence microscopy we observed
471 infection-associated fragmentation of membranes labelled with the *cis*-Golgi and *trans*-Golgi network
472 components GM130 and TGN46, respectively, in U2OS cells (**Fig. 6 and 7**). It would be interesting in
473 the future to use fluorescent markers and correlative cryoSIM plus cryoSXT imaging to identify precisely
474 which cellular compartments are found with an increased concentration at the juxtanuclear region of
475 HSV-1 infected cells [32,82].

476 In addition to an increase in the number of vesicles, we observed a significant increase in the median
477 size of lipid droplets during early but not late stages of infection when compared to uninfected cells (**Fig.
478 4C**). This observation is similar to a recent study that demonstrated EGFR-mediated upregulation of
479 lipid droplets early in HSV-1 infection (8 hpi) and an increase in lipid droplet size when cells were
480 exposed to dsDNA [83]. Furthermore, the authors of this study demonstrated that accumulation of lipid
481 droplets is transient, returning to baseline within 72 hours following stimulation of cells with dsDNA [83].
482 While we also observe a transient increase in lipid droplet size following HSV-1 infection, we did not
483 observe a striking increase in the number of lipid droplets per cryoSXT tomogram. However, we note

484 that in our study we infected U2OS cells whereas the previous work used HSV-1–infected primary
485 astrocytes. The authors observed that the increase in size of lipid droplets upon stimulation with dsDNA
486 is cell-type specific, with no increase being observed in THP-1 cells; it is similarly possible that U2OS
487 cells could have a larger number of lipid droplets in the resting state such that the absolute abundance
488 of lipid droplets is not increased in response to HSV-1 infection. An increase in lipid droplet size has
489 also been observed for human cytomegalovirus, a related herpesvirus, after infection for 1–4 days
490 [84,85]. Lipid droplets are important cell signalling platforms that have been shown to modulate the anti-
491 viral immune response during infection [83]. The high resolution of cryoSXT when compared with
492 confocal microscopy, combined with the high contrast afforded by carbon-rich lipid droplets, makes
493 cryoSXT imaging particularly suitable for future research into the link between lipid droplet size and
494 cellular innate immune responses.

495 We observed that mitochondria became more elongated and branched as infection progresses, in some
496 cases forming extensive networks (**Fig. 5**). Branching of mitochondria can either occur via *de novo*
497 synthesis or by fusion of mitochondria [24,86], and there are several possible explanations for the
498 change in mitochondrial morphology observed during HSV-1 infection. Mitochondrial movement tends
499 to occur along microtubules and this movement influences mitochondrial fusion/fission dynamics.
500 Fission can arise from divergent movement of mitochondrial extensions along microtubules and fusion
501 is supported by convergent movement of mitochondria [87]. Nocodazole treatment to depolymerize
502 microtubules blocks transport, fusion and fission of mitochondria, and there is evidence that thin
503 microtubule extensions develop when fission is obstructed [88]. It is possible that fission of existing
504 mitochondrial networks may be obstructed when microtubules depolymerize during HSV-1 infection,
505 and this may prevent the generation of small mitochondria. Such changes to the microtubule network
506 begin at 6 hpi and would thus be expected to have a greater influence on mitochondrial morphology in
507 the late stages of infection [25], consistent with our observations. Alternatively, the morphological
508 changes to mitochondria may reflect a cellular response to increased respiratory demand [89]. An
509 increase in ATP production can be achieved by mitochondrial elongation, for example under conditions
510 of stress such as hypoxia and starvation of glucose metabolism [19,20]. An increase in respiration,
511 including oxidative phosphorylation, has been observed during human cytomegalovirus infection [90].
512 An increased number of elongated mitochondria in cells at late stages of infection could increase ATP
513 production during infection. Increased oxidative stress provides a third plausible explanation for the

514 observed changes in mitochondrial morphology. Production of reactive oxygen species (ROS) during
515 respiration appears to be a common feature of viral infection that has been observed for hepatitis C
516 virus, respiratory syncytial virus and the herpesvirus Epstein-Barr virus [21–23]. One mechanism by
517 which the cell responds to oxidative stress is by fusion of undamaged and ROS-damaged mitochondria
518 to allow for compensatory effects by sharing resources needed for ATP production [24]. It is possible
519 that changes in mitochondrial morphology we observed may have arisen via enhanced fusion in
520 response to increased oxidative stress during infection.

521 Although a change in energy metabolism may reflect a generalized response by the cell to infection,
522 mitochondrial elongation has been observed during infection with other viruses (such as dengue virus)
523 that inhibit mitochondrial fission [91]. Several HSV-1 proteins have been reported to localize at
524 mitochondria (pUL7, pUL16, pUS3, pUL12.5), suggesting that HSV-1 directly modulates mitochondrial
525 activity [92–95]. pUS3 inhibits the activity of electron transport chain complexes II and III as early as 6
526 hpi [93] and pUL12.5 functions in the depletion of mitochondrial DNA and downregulation of
527 mitochondrial proteins, including ND6 and COX2, as early as 4–8 hpi [94]. The functional consequences
528 of pUL16 binding mitochondria are not well characterized, although we note that a pUL16 mutant co-
529 localizes with mitochondrial fission sites [95]. The precise mechanisms by which HSV-1 alters the
530 architecture of mitochondria and the role of specific viral proteins, versus virus-induced metabolic strain,
531 thus remains unclear. Combining metabolic profiling of infected cells with ultrastructural analysis of
532 mitochondrial morphology, using wild-type and mutant (knock-out) viruses, will help illuminate the
533 factors that drive the dramatic remodelling of mitochondria observed during HSV-1 infection and the
534 functional consequences thereof.

535 In conclusion, we have demonstrated that cryoSXT produces quantitative high-resolution 3D data for
536 biological research by studying the ultrastructural changes to cellular compartments induced during
537 HSV-1 infection. CryoSXT allows the detection of HSV-1 capsids and virions in distinct subcellular
538 locations, such as the nucleus, perinuclear space, cytoplasmic vesicles, and cell surface. Use of the
539 timestamp HSV-1 reporter virus facilitated identification of individual cells at early or late stages of
540 infection. In these subpopulations we observed accumulation of vesicles at juxtanuclear assembly
541 compartments, a transient increase in the size of lipid droplets, and elongation plus branching of
542 mitochondria as infection progresses. The ability of cryoSXT to image the entire depth of infected cells

543 in a near-native state, with minimal sample processing, highlights its utility as a tool for 3D imaging to
544 identify changes in cellular architecture that accompany virus infection.

545

546 **Materials & Methods**

547 *Reagents*

548 250 nm gold colloid fiducials were purchased from BBI Solutions (EM.GC250, batch 026935). The
549 working mixture was prepared via sedimentation of 1 mL of stock solution by centrifugation (12×g, 5
550 mins, RT) and then resuspending the pellet in 50 µL Hanks' Balanced Salt Solution (HBSS; Thermo
551 Fisher). The fiducials were sonicated at 80 kHz (100% power) and 6°C to prevent aggregation. 3 mm
552 gold EM finder grids with a perforated carbon film (R 2/2, 200 mesh) were purchased from Quantifoil
553 (AU G200F1 finder, batches Q45352 & Q45353). Poly-L-lysine was purchased from Sigma Aldrich.

554 *Cell Lines*

555 Mycoplasma-free U2OS cells (ATCC HTB-96; RRID CVCL_0042) and human foreskin fibroblast cells
556 immortalized with human telomerase reverse transcriptase (HFF-hTERT cells)[96] were cultured in
557 Dulbecco's Modified Eagle's Medium (DMEM; Thermo Fisher) supplemented with 10% (v/v) foetal
558 bovine serum (FBS; Capricorn), 2 mM L-glutamine (Thermo Fisher), and 100 U/mL
559 penicillin/streptomycin (Thermo Fisher). HBSS and 0.25% Trypsin-EDTA (Thermo Fisher) were used
560 to wash and detach adherent cells, respectively. Cells were maintained in a humidified 5% CO_2
561 atmosphere at 37°C.

562 *Biosafety Measures*

563 All cells and viruses were handled according to containment level 2 (CL2) guidelines and a risk
564 assessment was carried out and approved by the Rutherford Appleton Laboratory (RAL) Health and
565 Safety Committee. EM grids containing cells and viruses were handled in appropriate microbiology
566 safety cabinets and forceps were regularly washed in 70% (v/v) ethanol. Personal protective equipment
567 in the form of lab coats, lab gloves, and goggles were worn to protect experimenters. All tissue-culture,
568 cryocooling, and imaging equipment was stored in CL2 laboratories.

569 *Recombinant Viruses*

570 Infections were performed using recombinant HSV-1 strain KOS expressing either the endogenously
571 tagged viral proteins eYFP-VP26 and gM-mCherry (**Fig. 1**) or the endogenously tagged viral proteins
572 eYFP-ICP0 and gC-mCherry (timestamp HSV-1, **Fig. 2–8** and **S1–4 Figs**)[16], to allow distinction

573 between early and late stages of infection in U2OS and HFF-hTERT cells, with the exception of the
574 leftmost panel in **Fig. 1I** for which a non-fluorescent wild-type HSV-1 strain KOS was used. Virus stocks
575 were prepared by infection of Vero cells at low MOI (0.01) for 3–5 days, until cytopathic effect was
576 evident, before scraping cells into the medium. The cells were frozen at -70°C, thawed and sonicated
577 at 50% amplitude for 40 seconds. Crude virus stocks were clarified by centrifugation at 3,200×g in a
578 benchtop centrifuge, aliquoted, and viral titers of the aliquots were quantified on Vero and U2OS cells
579 as described previously [97].

580 *Infection Assays*

581 For widefield imaging under cryogenic conditions and cryoSXT, EM grids were glow discharged and
582 treated with filtered poly-L-lysine for 10 minutes as described previously [33]. 3×10^5 U2OS or HFF-
583 hTERT cells per well were seeded in 6-well plates containing the treated EM grids and were incubated
584 overnight. Subsequently, the cells were infected with timestamp HSV-1 at an MOI of 1–3. For widefield
585 microscopy of timestamp HSV-1 to measure the progression of replication over time, U2OS and HFF-
586 hTERT cells were allowed to grow overnight following seeding in 6-well plates at 2×10^5 cells per well
587 (**Fig. 2A**) or on borosilicate coverslips in 12-well plates at 1×10^5 cells per well (**Fig. 2B**). The cells were
588 infected with the recombinant HSV-1 with an MOI of 1–3. For SIM and confocal microscopy, U2OS cells
589 were seeded on borosilicate coverslips in 12-well plates overnight at 1×10^5 cells per well. The cells
590 were infected with the recombinant HSV-1 with an MOI of 3. The time of inoculation was designated
591 the start time of infection. For all infections, to maximize adsorption of virus, cells were incubated in a
592 low volume of medium (250 µL/well in 12-well plates and 500 µL/well in 6-well plates) for 1 hour in a
593 humidified 5% CO_2 atmosphere at 37°C and the plates were swirled every 15 minutes. For widefield
594 imaging under cryogenic conditions and cryoSXT, the medium was topped up to 2 mL and the samples
595 were incubated for 9 hours alongside uninfected controls, except for the samples in **Fig. 1**, which were
596 incubated for 16 hours. The EM grids were overlayed with 2 µL of the gold fiducial working mixture as
597 described in the *Reagents* section. A Leica EM GP2 plunge freezer was used to blot the grids for 0.5–
598 1 s at 30°C and 80% humidity. The grids were then plunged into liquid nitrogen-cooled liquid ethane
599 and transferred into liquid nitrogen storage before imaging. For the timestamp HSV-1 images (**Fig. 2A**),
600 the inoculum was diluted to 2 mL with medium for the remainder of the incubation (9–24 hours). For the
601 experiments measuring the progression of timestamp HSV-1 replication over time (**Fig. 2B**), media was

602 aspirated after the 1 hour of incubation and the cells were treated for 1 min with citric acid (40 mM citric
603 acid pH 3, 135 mM NaCl, 10 mM KCl) to inactivate unabsorbed virus. Cells were then washed thrice
604 with PBS and then overlain with 500 µL of fresh medium before incubation for a further 2–24 hours. For
605 confocal microscopy and SIM, the media were topped up to 1 mL for the remainder of the incubation
606 (see figure legends for varied time points). For cells stained with MitoTracker Deep Red FM (Thermo
607 Fisher), the media was aspirated 30 minutes before fixation and washed twice with serum-free media.
608 50 nM MitoTracker in serum-free media was added to the cells for 30 minutes. For all samples not
609 prepared on EM grids, the cells were washed twice with HBSS or PBS and were fixed with 4% (v/v)
610 formaldehyde for 20 minutes, followed by three HBSS/PBS washes. For confocal microscopy and SIM,
611 the cells were washed twice with PBS, permeabilised with 0.1% saponin in PBS for 30 minutes at room
612 temperature on a rocking platform and were blocked for 30 minutes with a PBS solution of 0.1% saponin
613 and 5% (v/v) FBS at room temperature on a rocking platform. The samples were stained with either
614 2.5 µg/mL mouse anti-human GM130 (Clone 35/GM130 (RUO), BD Biosciences, RRID: AB_398142),
615 10 µg/mL mouse anti-human TGN46 (SAB4200355, Merck), or a 1 in 20 dilution of rat anti-β-tubulin
616 (clone YL1/2) hybridoma supernatant [98] in blocking solution, washed, then stained with 4 µg/mL goat
617 anti-mouse Alexa Fluor 647 antibody (A-21235, ThermoFisher) in blocking solution, washed and
618 mounted using ProLong Gold containing DAPI (P36930, ThermoFisher).

619 *Widefield Microscopy*

620 For room temperature samples, a Zeiss AxioImager2 microscope with an achromatic 50× air objective
621 (Zeiss LD EC Epiplan-Neofluar 50x/0.55 DIC M27; NA=0.55) was used to image fixed infected cells
622 grown on plastic 6-well plates. Fluorescent images were collected using the Zeiss 46 HE YFP filter
623 (Excitation 500±25 nm, Emission 535±30 nm) and the Zeiss 64 HE mPlum filter (Excitation 587±25 nm,
624 Emission 647±70 nm). For cryo-widefield microscopy, cells at early- and late-stages of infection were
625 identified based on the spatiotemporal expression of eYFP-ICP0 and gC-mCherry using a Zeiss
626 AxioImager2 microscope with an achromatic 50× objective as described above. A liquid nitrogen
627 cryostage (Linkam Scientific) was used to maintain the samples at 77 K. Each grid was mapped in its
628 entirety in the brightfield and fluorescent channels (as above) using LINK (Linkam Scientific).

629 *Cryo-Soft-X-Ray Tomography*

630 X-ray images were collected using an UltraXRM-S/L220c X-ray microscope (Carl Zeiss X-ray
631 Microscopy) at beamline B24 at the UK synchrotron Diamond Light Source. Grids were imaged in a
632 liquid nitrogen-cooled vacuum chamber and samples were illuminated with 500 eV X-rays (λ = 2.48 nm)
633 for 0.5 or 1 s per projection. The transmitted light was focused by diffraction using zone plate objectives
634 with nominal resolution limits of either 25 nm or 40 nm. The 25 nm zone plate offers higher resolution
635 but captures a smaller field of view (~10×10 µm) than the 40 nm zone plate (~16×16 µm). Only one
636 zone plate can be installed in the microscope and the zone plate is not user changeable. The installed
637 zone plate differed across the beam time allocations use for this study, with all images being collected
638 using the 25 nm zone plate except for **Fig. 1 C, D, and G–I**, for which the 40 nm zone plate was used.
639 Transmitted images were collected using a 1024B Pixis CCD camera (Princeton instruments). X-ray
640 mosaic images (7×7 images capturing 66.2×66.2 µm for the 25 nm objective and 106.0×106.0 µm for
641 the 40 nm objective) were collected from different areas on the grid to assess overall cell morphology.
642 For identification of early and late stages of infection, X-ray mosaics were compared with fluorescent
643 scans acquired on the cryo-widefield microscope to identify specific infected cells. These mosaics were
644 also used to identify regions of interest for tomography. Tilt series of projections were collected from
645 these regions by rotating the sample around an axis normal to the incident X-ray beam by up to 140°
646 in increments of 0.2° or 0.5° per image, with maximum tilt angles of −60°/+60° and −70°/+70° for the
647 25nm and 40nm objective, respectively. SXT tilt series were processed using IMOD (version 4.9.2)[42].
648 The images were aligned along a single axis. A coarse alignment was performed by cross-correlation
649 with a high frequency cut-off radius of 0.1. Coarsely aligned tilt series were further aligned manually
650 using gold fiducials and dark cellular compartments, such as lipid droplets. A boundary model was
651 generated to reorient the 3D data in case the sample was collected at an angle and final alignment was
652 performed using linear interpolation. Tomograms were generated using back projection followed by 20
653 iterations of a simultaneous iterations reconstruction technique (SIRT)-like filter to reduce noise.

654 *Structured Illumination Microscopy and Deconvolution*

655 A custom, three-colour SIM microscope [99] was used to collect images. A ferroelectric binary Spatial
656 Light Modulator (SLM) (SXGA-3DM, Forth Dimension Displays) was used to pattern the light with a
657 grating structure (3 angles and 3 phases). Light was collected by a 60× water immersion objective with

658 a NA of 1.2 (UPLSAPO60XW, Olympus) and a sCMOS camera (C11440, Hamamatsu). eYFP-ICP0
659 fluorescent emission was captured using a 488 nm laser (iBEAM-SMART-488, Toptica) and an BA510-
660 550 (Olympus) emission filter. gC-mCherry fluorescence was captured using a 561 nm laser (OBIS561,
661 Coherent) and a BrightLineFF01-600/37 filter (Semrock). AF647 fluorescence was captured using a
662 640 nm laser (MLD640, Cobolt) and a BrightLineFF01-676/29 filter (Semrock). Background-reduced
663 and resolution-enhanced images were reconstructed from raw SIM data using FairSIM [100].
664 Deconvolution was performed alongside using a Richardson-Lucy algorithm with 5 iterations. 100 nm
665 beads (TetraSpeck Microspheres, Thermo Fisher) were used to determine the shifts in X and Y for
666 channel alignment. The channels were aligned using the TransformJ plugin in Fiji [101].

667 *Confocal microscopy*

668 A Zeiss LSM700 inverted confocal AxioObserver.Z1 microscope was used at room temperature to
669 capture images with ZEN software (Zeiss). A 100× apochromatic objective with oil immersion and
670 pinhole set to 1 airy unit was used to collect images. Z stacks containing 1024×1024 pixels at 400 nm
671 increments were captured within a 16-bit unsigned range using 8-fold line averaging. Maximum Z
672 projections were generated using Fiji [101].

673 *Segmentation*

674 Mitochondria were segmented using *Contour*, a bespoke semi-automated segmentation and
675 quantitation tool developed with Python 3 (full details on *Contour* can be found in [60]). Briefly, *Contour*
676 automatically segments high contrast features such as mitochondria by thresholding and then applying
677 a restriction on the minimum number of consecutive segmented pixels vertically and horizontally. Next,
678 gaps in the segmented volume can be filled in by running this algorithm in local regions of interest.
679 Separate elements in the segmented volume are differentiated by grouping of neighbouring voxels
680 together. The differentiated elements are colour-coded and their volumes are quantitated from the
681 number of voxels. The edges of the segmented elements are smoothened in each image plane by
682 translating the image by one pixel in all eight cardinal and ordinal directions in the XY plane and
683 calculating the median pixel value for all these translations. A 3D Gaussian filter with a sigma of 2 was
684 also added using Fiji to further smoothen the elements [101]. In *Contour*, the width of each segmented
685 element was calculated by finding all the coordinates of voxels at the perimeter of segmented elements
686 and calculating the largest modulus between any two coordinates. Segmented volumes of cytoplasmic

687 vesicles were generated manually using the Segmentation Editor 3.0.3 ImageJ plugin [101] and these
688 were imported into *Contour* to differentiate between segmented elements and quantitate the width of
689 the vesicles. Segmented volumes were visualized in 3D using the 3D Viewer plugin in ImageJ [101].
690 Cytoplasmic vesicles were segmented from 12 well-reconstructed X-ray tomograms lacking X-ray
691 damage. Lipid droplets were automatically segmented from 94 tomograms using *Contour* from 8-bit
692 tomograms. Tomograms were excluded from segmentation if they were poorly reconstructed, were
693 subjected to X-ray damage, or were from thick sections and contained out-of-focus lipid droplets in
694 some projection planes. Given that gold fiducials and lipid droplets have similar projection intensities in
695 8-bit images, gold fiducials were also included in the automatic segmentation. During curation of the
696 segmented volumes, gold fiducials were manually erased. This was possible because they are easy to
697 distinguish from lipid droplets based on the higher intensity of their missing wedge artefacts. The
698 projection intensities of lipid droplets and gold fiducials are lower than other material in the tomograms,
699 including noise, and they could thus be segmented based purely on threshold values without applying
700 a width restriction. This prevented the exclusion of very small lipid droplets. Volumes were calculated
701 in *Contour* for each lipid droplet. Lipid droplets that could not be individually resolved or were cut off at
702 the edges of tomograms were excluded from the analysis.

703 *Graphs and statistics*

704 Distributions of capsid and virion widths were illustrated using a Violin SuperPlot [102], with data
705 grouped by source tomograms. The stacked area plots for the proportion of infected cells at different
706 stages of infection were generated using the ggplot2 package [103] in R studio [104]. The distribution
707 of vesicle widths were illustrated using a SuperPlot [105], with data grouped by source tomograms. The
708 numbers of mitochondrial branch points (branching nodes) were illustrated using a Violin SuperPlot
709 [102], with data grouped by replicate. A two-tailed paired t-test was used to compare the width of the
710 nuclear envelope at a site of primary envelopment with the width of the nuclear envelope elsewhere on
711 the same tomogram using Excel (Microsoft). The t-test was two-tailed because we observed a normal
712 distribution of widths and it was paired because the two data points (width of nuclear envelope at
713 perinuclear viral particle and in nearby region) were collected from the same tomogram. The variance
714 in the width of the extracellular virions was greater than four times the variance in the width of nuclear
715 capsids. As a result, a Mann-Whitney *U* test for unequal variance was used to assess the significance

716 of the difference in width of capsids and virions using R Studio [104]. To assess significance of
717 differences in mean vesicle widths, a one-way ANOVA and Tukey tests were performed using Prism
718 version 8.2.1 (GraphPad Software). These tests were used instead of t tests to avoid the higher risk of
719 type I errors associated with performing multiple t tests on more than two conditions. For the same
720 reason, one-way ANOVA and Tukey tests were used to assess significant differences in the number of
721 mitochondrial branching nodes (using R Studio [104]). The data distributions for the lipid droplet
722 volumes were positively skewed and median volumes were chosen for further analysis because they
723 are less affected by extreme values than means. Owing to the skew, Mann-Whitney *U* tests were used
724 to determine significance of differences between conditions for the lipid droplet volumes. The
725 tomograms used to quantitate the number of branching nodes were selected according to the following
726 criteria. Firstly, we excluded tomograms that were poorly reconstructed (e.g. due to displacement of the
727 rotational axis during data collection or due to a lack of fiducials or lipid droplets for image alignment).
728 Next, we only included tomograms in which the mitochondria were well dispersed throughout the field
729 of view to ensure that we didn't systematically underestimate the number of branching nodes by
730 including tomograms where only small fragments of individual mitochondria were visible, for example
731 in the corners of the field of view. Finally, we excluded tomograms that contained swollen mitochondria
732 because this was taken to indicate that the cells might be undergoing apoptosis, a process known to
733 cause significant alteration to mitochondrial morphology [61]. We assessed an equal number of
734 tomograms for each replicate and condition to avoid introducing unequal variance into our ANOVA test.

735

736 **Acknowledgements**

737 We thank Diamond Light Source for access to beamline B24 (via response mode applications mx18925,
738 mx19958, bi21485 and bi23508) and the experimental hall coordinators for helpful support. We thank
739 members of beamline B24 at the Diamond Light Source (Mohamed Koronfel, Ilias Kounatidis, Chidinma
740 Okalo, and Matt Spink) for technical support with cryoSXT. We thank João Ferreira Fernandes
741 (University of Oxford) and Thomas Fish (Diamond Light Source) for help with the development of
742 *Contour*. We thank David Carpentier (University of Cambridge) for technical support with confocal
743 microscopy. We thank Harriet Groom (University of Cambridge) for reading and advising on the
744 manuscript. For the purpose of Open Access, the authors have applied a CC BY public copyright licence
745 to any Author Accepted Manuscript (AAM) version arising from this submission.

746 **Data Availability**

747 Original imaging data for tomograms illustrated in the manuscript are deposited with the University of
748 Cambridge Apollo Repository, available at https://doi.org/10.17863/CAM.78593. Representative
749 tomograms have also been published in the EMPIAR repository (EMBL-EBI) with the accession number
750 EMPIAR-10972.

751 **Financial Disclosure is as follows:**

752 This work was supported by a PhD studentship co-funded by Diamond Light Source and the
753 Department of Pathology, University of Cambridge, to KLN, by a research fellowship from the Deutsche
754 Forschungsgemeinschaft (SCHE 1672/2-1) to KMS, by the funding from the Engineering and Physical
755 Sciences Research Council (EP/H018301/1) and the Medical Research Council (MR/K015850/1 and
756 MR/K02292X/1) to CFK, by a Biotechnology and Biological Sciences Research Council Research Grant
757 (BB/M021424/1) to CMC, and by a Sir Henry Dale Fellowship, jointly funded by the Wellcome Trust and
758 the Royal Society (098406/Z/12/B) to SCG.

759 **Competing Interests**

760 The authors declare that they have no conflict of interest.

761 **Table 1. Collection of cryoSXT data to analyse changes in cellular morphology accompanying**
762 **infection.** CryoSXT data was collected using a 25 nm zone plate from multiple uninfected cells or cells
763 at early and late stages of infection across three independent replicates. Tiled X-ray projections ('X-ray
764 mosaics') with a 66.2×66.2 μm field of view were collected at multiple areas on the sample grid to
765 identify cells of interest. Tilt series were collected at perinuclear or peripheral regions of the cytoplasm
766 within these cells and were processed to generate tomograms.

Replicate	Stage of infection	X-ray mosaics	Cells in mosaics	Cells imaged by tomography	Tomograms
1	Uninfected	19	30	18	29
	Early	4	4	2	4
	Late	8	13	10	14
2	Uninfected	10	20	14	20
	Early	9	13	11	13
	Late	10	10	8	12
3	Uninfected	8	27	26	27
	Early	6	7	5	5
	Late	8	13	13	15

767

768

769

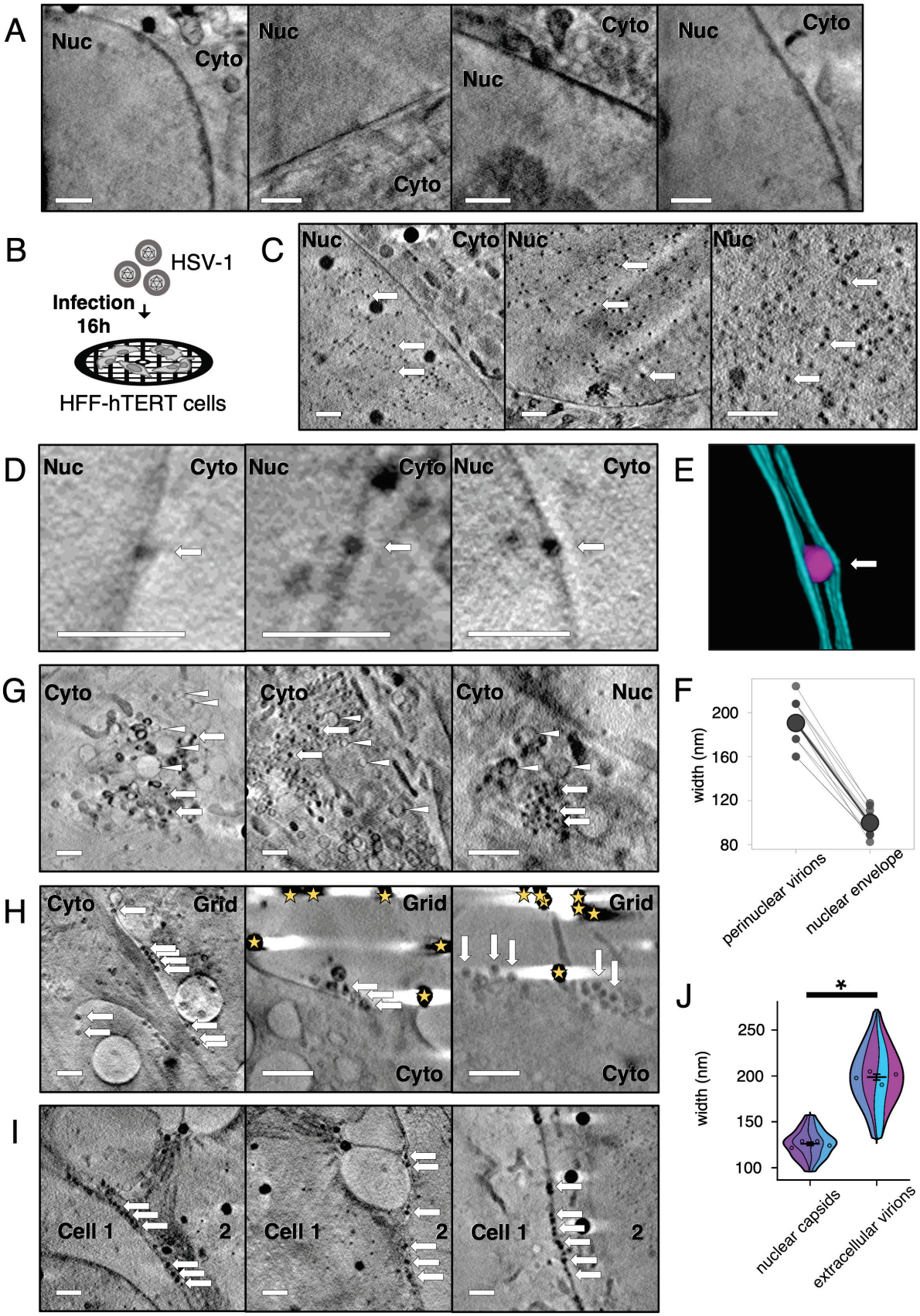

770 **Fig. 1. Soft X-ray tomography imaging at cryogenic temperatures of HSV-1-infected HFF-hTERT**

771 **cells identifies virus particles.** HFF-hTERT cells were grown on EM grids, infected (MOI 2) with

772 HSV-1 or mock-infected, and plunge cryocooled 16 hpi. All tomograms were reconstructed from X-ray
773 projections collected using 25 nm (**A**) or 40 nm (**C, D, G–I**) zone plate objectives; scale bars = 1 µm.
774 (**A**) The nucleus (Nuc) has a largely uniform X-ray absorbance in uninfected HFF-hTERT cells. Cyto,
775 cytoplasm. (**B**) Schematic of infection workflow. (**C**) In HSV-1 infected cells many dark puncta are
776 evident in the nucleus, consistent with these puncta being newly assembled HSV-1 capsids. (**D**) Dark
777 puncta were also observed within the perinuclear space of the nuclear envelope, consistent with these
778 being HSV-1 capsids undergoing primary envelopment/de-envelopment to leave the nuclear space. (**E**)
779 Segmentation of a perinuclear viral particle (magenta) and the two membranes of the nuclear envelope
780 (cyan). The perinuclear viral particle expands the nuclear envelope. (**F**) The width of perinuclear viral
781 particles plus associated membranes is 190.5 ± 6.01 nm SEM (N=11; 20.8 nm SD), which is greater
782 than the width of the nuclear membrane elsewhere (99.8 ± 3.57 nm SEM; N=11; 11.9 nm SD). (**G**) HSV-
783 1 capsids (arrows) were also observed in the cytoplasm alongside vesicles (arrowheads). (**H**) Multiple
784 particles are observed along the surface of infected cells, consistent with these being assembled HSV-
785 1 virions that have exited the infected cell. Gold fiducials are indicated with stars. (**I**) HSV-1 virions are
786 also observed at the junctions between cells. (**J**) The width of the nuclear capsids is 125.8 ± 1.70 nm
787 SEM (n=80 from 4 tomograms), consistent with these being HSV-1 capsids (~125 nm)[38,106]. The
788 width of the extracellular virions is 198.6 ± 3.48 nm SEM (n=80 from 4 tomograms), consistent with
789 these being fully-enveloped HSV-1 virions (~200 nm)[51]. Due to unequal variance, a Mann-Whitney *U*
790 test was performed to determine a significant difference in the width of nuclear capsids and extracellular
791 virions (W=126, p-value$<2.2\times10^{-16}$). Error bars show mean ± SEM.

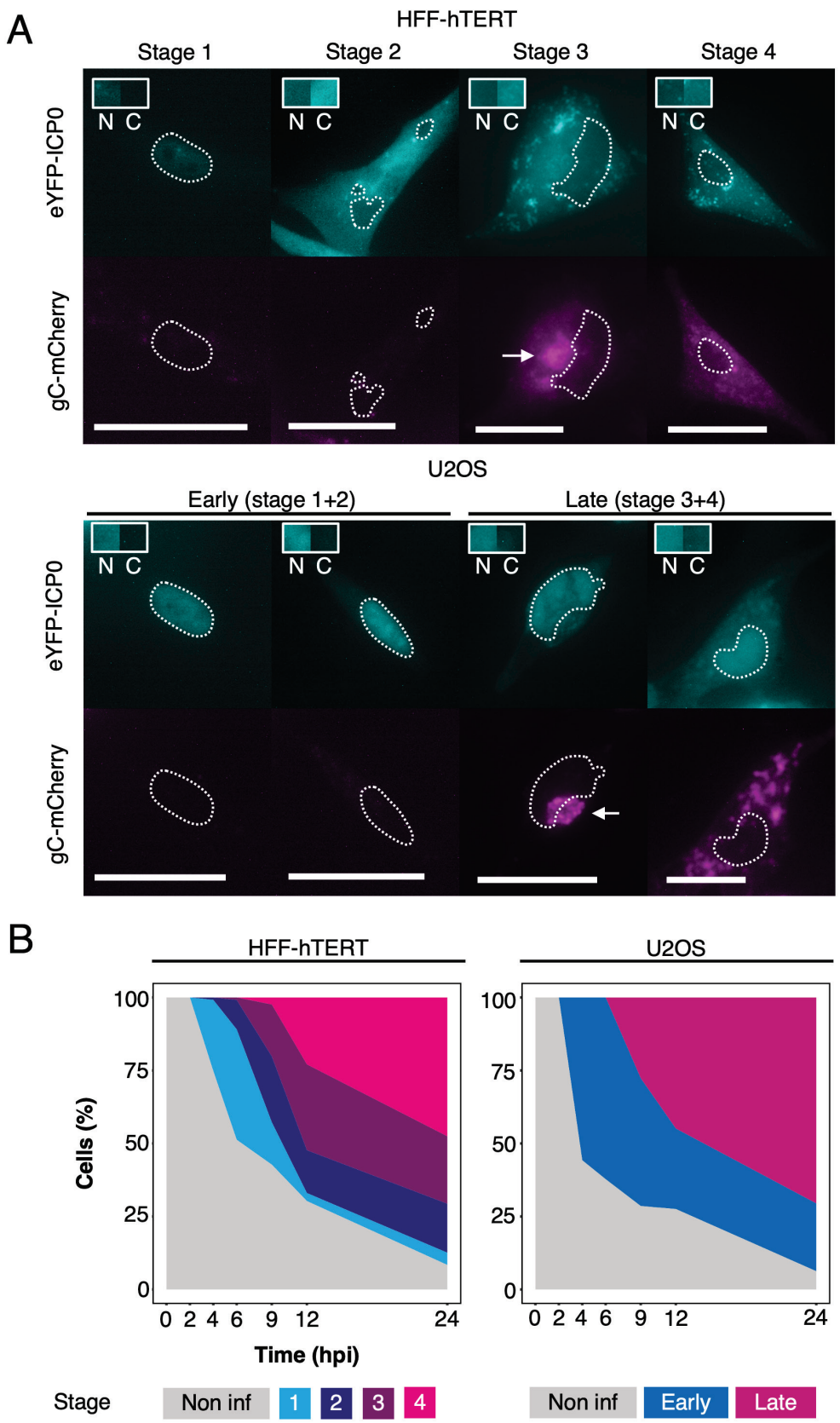

792

793 **Fig. 2. Temporal analysis of HSV-1 infection using the dual-fluorescent timestamp virus.** (**A**)

794 Room temperature widefield fluorescence imaging of timestamp HSV-1 infected HFF-hTERT and

795 U2OS cells was used to delineate between stages of infection based on the expression and localization
796 of the early protein eYFP-ICP0 and the late protein gC-mCherry [16]. The spatiotemporal expression of
797 these fusion proteins was similar in HFF-hTERT and U2OS cells, except for increased retention of
798 eYFP-ICP0 in the nucleus of U2OS cells during all stages. Outlines show the nuclei and arrows indicate
799 juxtanuclear compartments rich in gC-mCherry. Scale bars = 50 μm. Boxes show a sample of the eYFP-
800 ICP0 intensity from the nucleus (N) and cytoplasm (C). (**B**) The proportion of infected cells in each stage
801 was determined using widefield imaging at 2, 4, 6, 9, 12, and 24 hpi following infection (MOI 3) of HFF-
802 hTERT and U2OS cells with timestamp HSV-1.

803

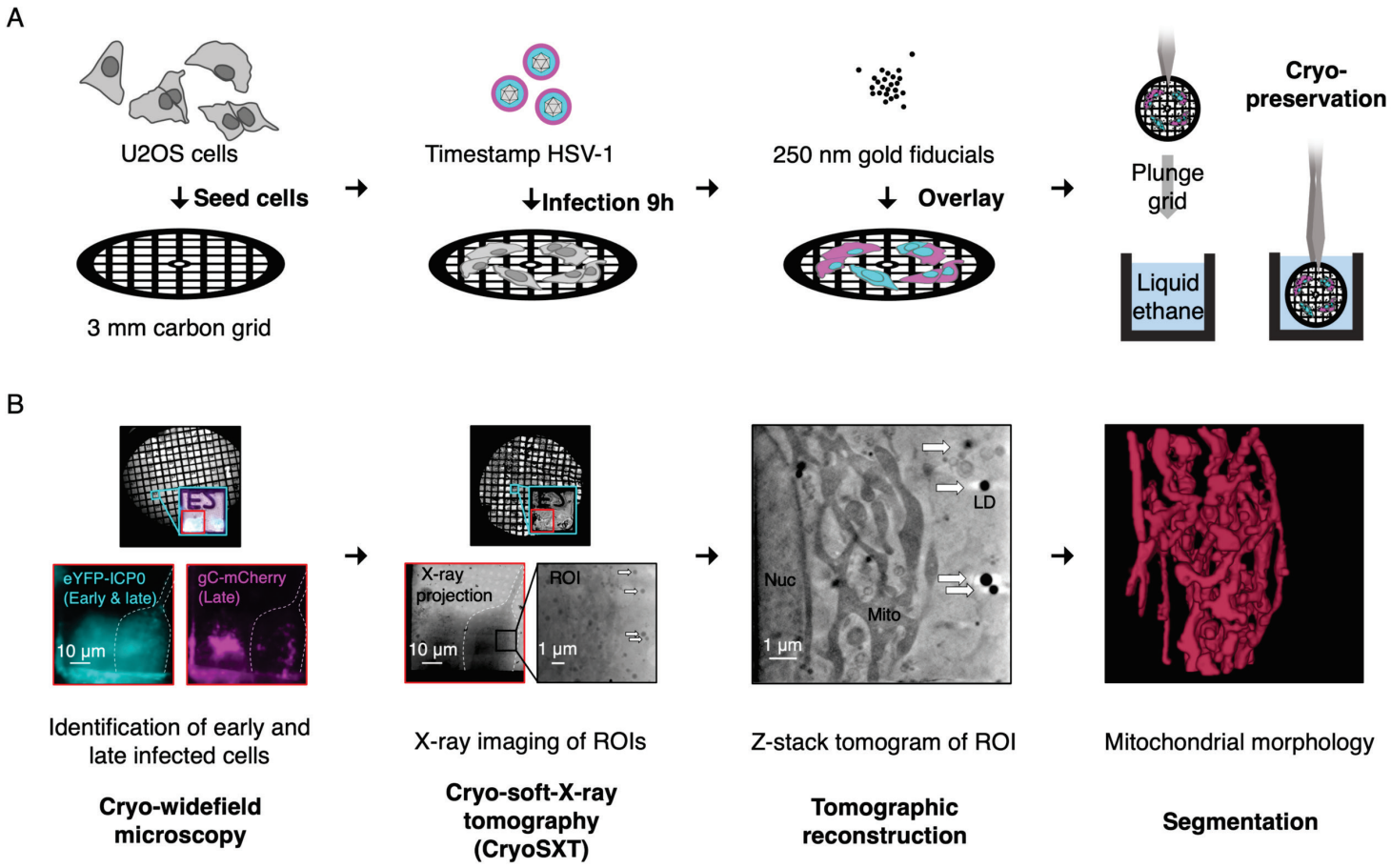

Fig. 3. Workflow for multi-modal imaging of HSV-1 infected cells. (**A**) Preparation of infected cells samples for multimodal imaging. U2OS cells are cultured on perforated EM grids and infected with recombinant 'timestamp' HSV-1, expressing fluorescently tagged proteins eYFP-ICP0 and gC-mCherry that allow identification of the stage of infection for each cell under investigation. At 9 hpi, gold fiducials are overlayed onto the sample to facilitate image registration and grids are cryopreserved in a near-native state by plunge cryocooling in liquid ethane. (**B**) Multi-modal imaging of infected U2OS cells. A widefield microscope with a cryo stage is used to locate the grid positions of infected cells. The stage of infection for each cell is determined based on the expression of eYFP-ICP0 and gC-mCherry (as shown in **Fig. 2**). These grids are then loaded into the cryo-soft-X-ray microscope at Diamond Light Source beamline B24 and are illuminated with soft X-rays at the marked grid positions. X-ray projections of regions of interest (ROIs) are collected at multiple angles and aligned using the gold fiducials and intracellular features, such as lipid droplets (LDs), with the program IMOD [42]. Tomograms are reconstructed from these projections using IMOD to compare intracellular morphology between uninfected cells and those at early- or late-stages of infection. Segmentation with tools like *Contour* [60] facilitates quantitation and visualization in three dimensions of the observed cellular structures.

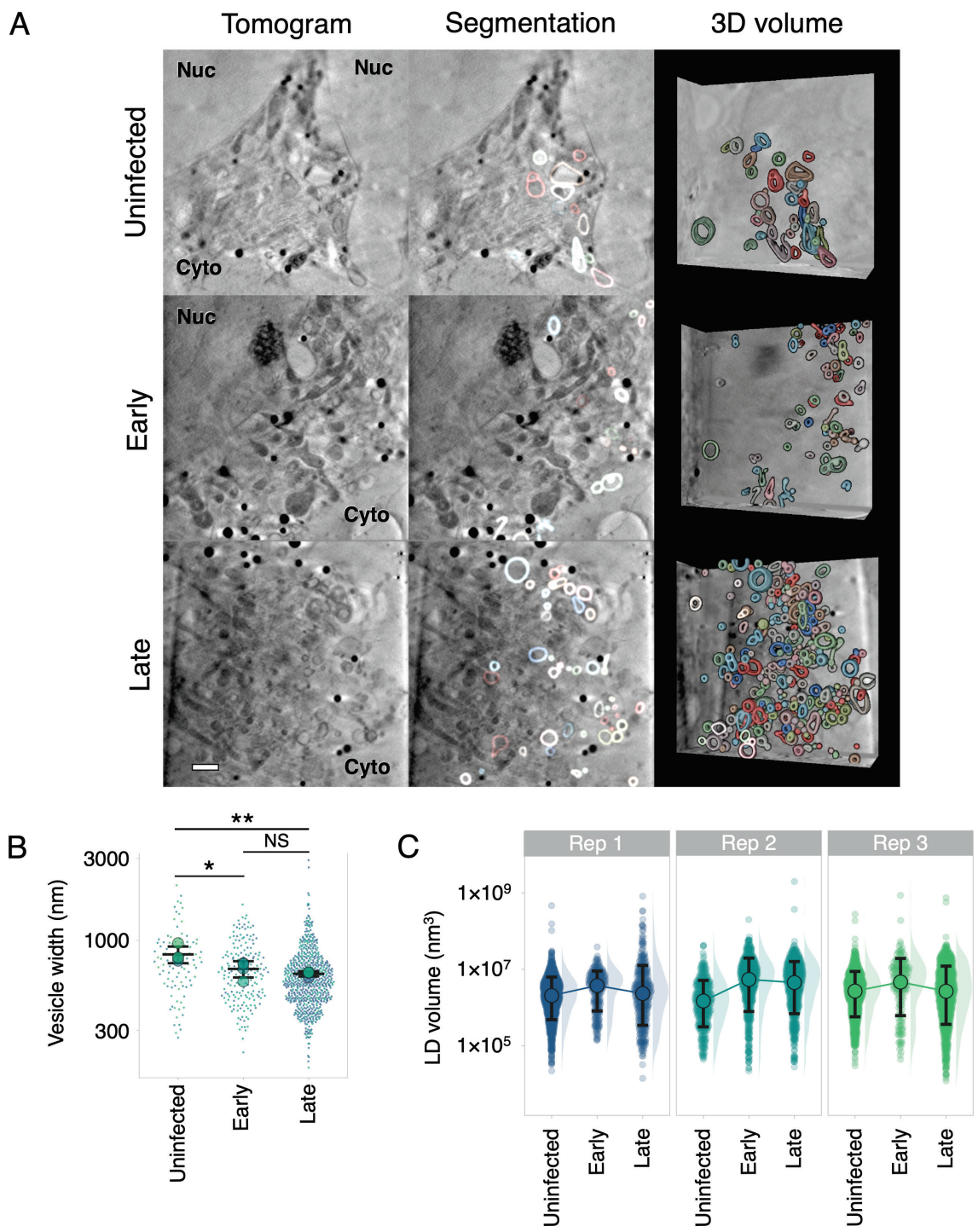

819

820 **Fig. 4. Remodelling of cytoplasmic vesicles during HSV-1 infection.** CryoSXT tomograms were
821 recorded from uninfected cells, or cells at an early or late stage of infection with timestamp HSV-1, as
822 determined via wide field fluorescence cryo-microscopy. Data are representative of three independent
823 experiments. Scale bar = 1 µm. (**A**) A higher concentration of vesicles is observed at the juxtanuclear

824 compartment in cells at early- or late-stages of infection compared with uninfected cells. (**B**) The
825 maximum width of each vesicle in three-dimensions was measured in *Contour* [60]. Width was
826 measured instead of volume because the segmented vesicles were open-ended owing to reduced
827 contrast in the tomograms of membranes normal to the incident X-ray beam. Vesicles with a spherical,
828 ellipsoidal, or dumbbell shape were included in the analysis but vesicles with a shape that didn't fall into
829 these categories were excluded. Intra-luminal vesicles and vesicles that were not individually resolved
830 by the segmentation were also excluded from the analysis. Significance of differences was assessed
831 with a one-way ANOVA and Tukey tests for the combinations: uninfected-early ($p=0.04$), uninfected-
832 late ($p=0.01$), and early-late ($p=0.62$). Big circles show the mean vesicle width per tomogram (4
833 tomograms per condition). Error bars show overall mean ± SD. (**C**) Lipid droplets were segmented and
834 measured using *Contour* [60] and their distributions were plotted on a logarithmic scale. Median
835 volumes ± SD (hollow circles plus error bars) are shown for each group because median values are
836 less affected than mean values by non-normal distributions. The median volume was highest in cells at
837 early stages of infection in all three replicates. A linear plot of the distributions and significance tests for
838 the lipid droplet volumes are shown in **S2 Fig**.

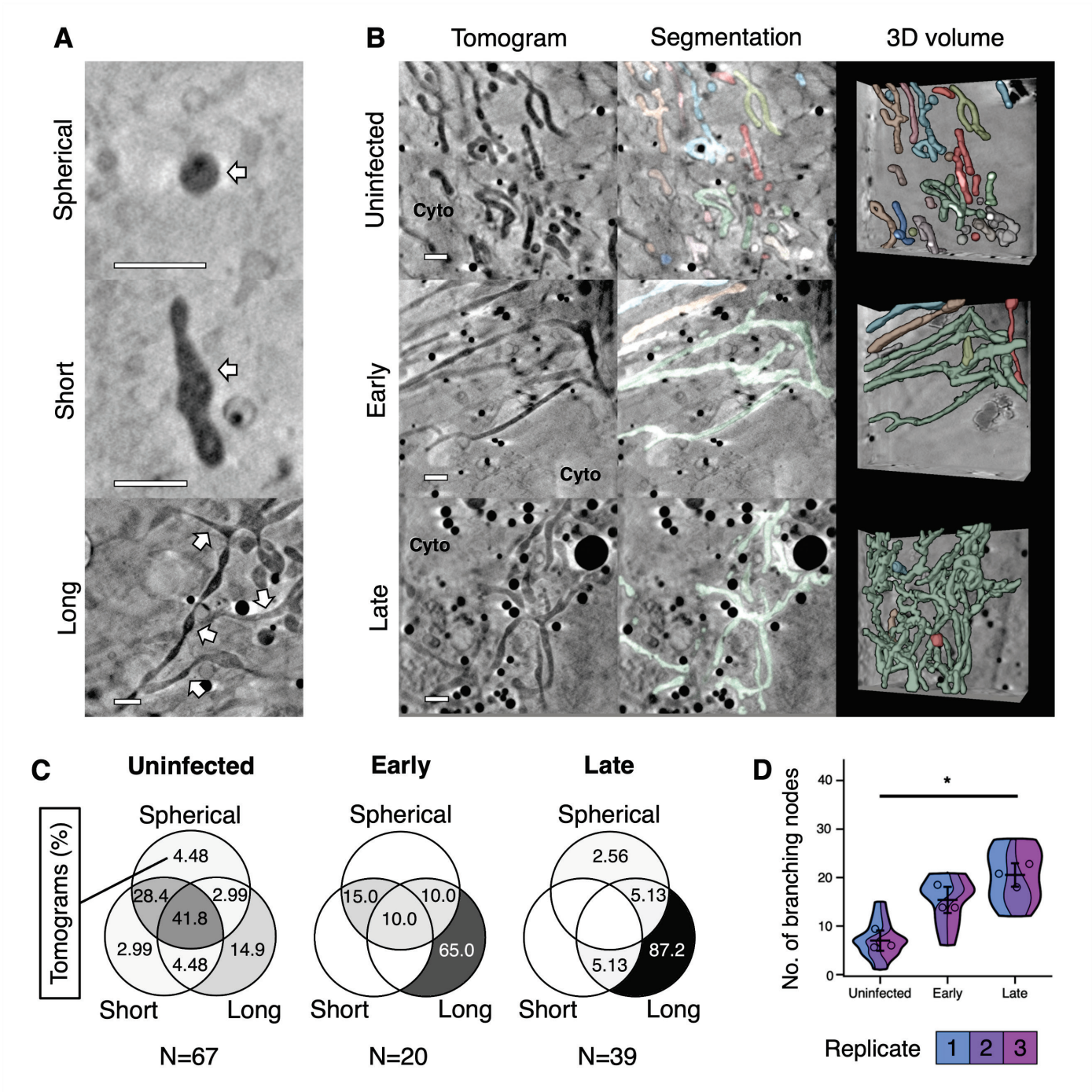

Fig. 5. Remodelling of mitochondria during HSV-1 infection. Morphological changes to mitochondria were assessed from cryoSXT tomograms collected from uninfected cells and cells at early- or late-stages of infection with timestamp HSV-1. Data are representative of three independent experiments. Scale bars = 1 µm. (**A**) Examples of spherical, short, and long mitochondria are indicated with white arrows. (**B**) A shift towards elongated and branched mitochondria was observed during infection. Mitochondria were segmented and differentiated using *Contour* [60] to highlight the abundance and 3D geometry of individual mitochondria. (**C**) Venn diagrams showing the percentage of tomograms at each stage of infection with Spherical, Short or Long mitochondria, or a combination of

847 these phenotypes. The percentages of tomograms with long mitochondria were greater for cells at
848 early- or late-stages of infection than for uninfected cells. Mitochondrial morphology was more
849 heterogenous in uninfected cells. Combined percentages from all replicates are shown here and Venn
850 diagrams for each replicate are shown in **Supp. Fig 2C**. (**D**) The numbers of branching nodes were
851 calculated for 45 tomograms across all replicates and significant differences in the number of nodes
852 between uninfected cells and those at late stages of infection were determined for each replicate using
853 ANOVA and Tukey tests ($p < 0.05$). Error bars show mean ± SD.

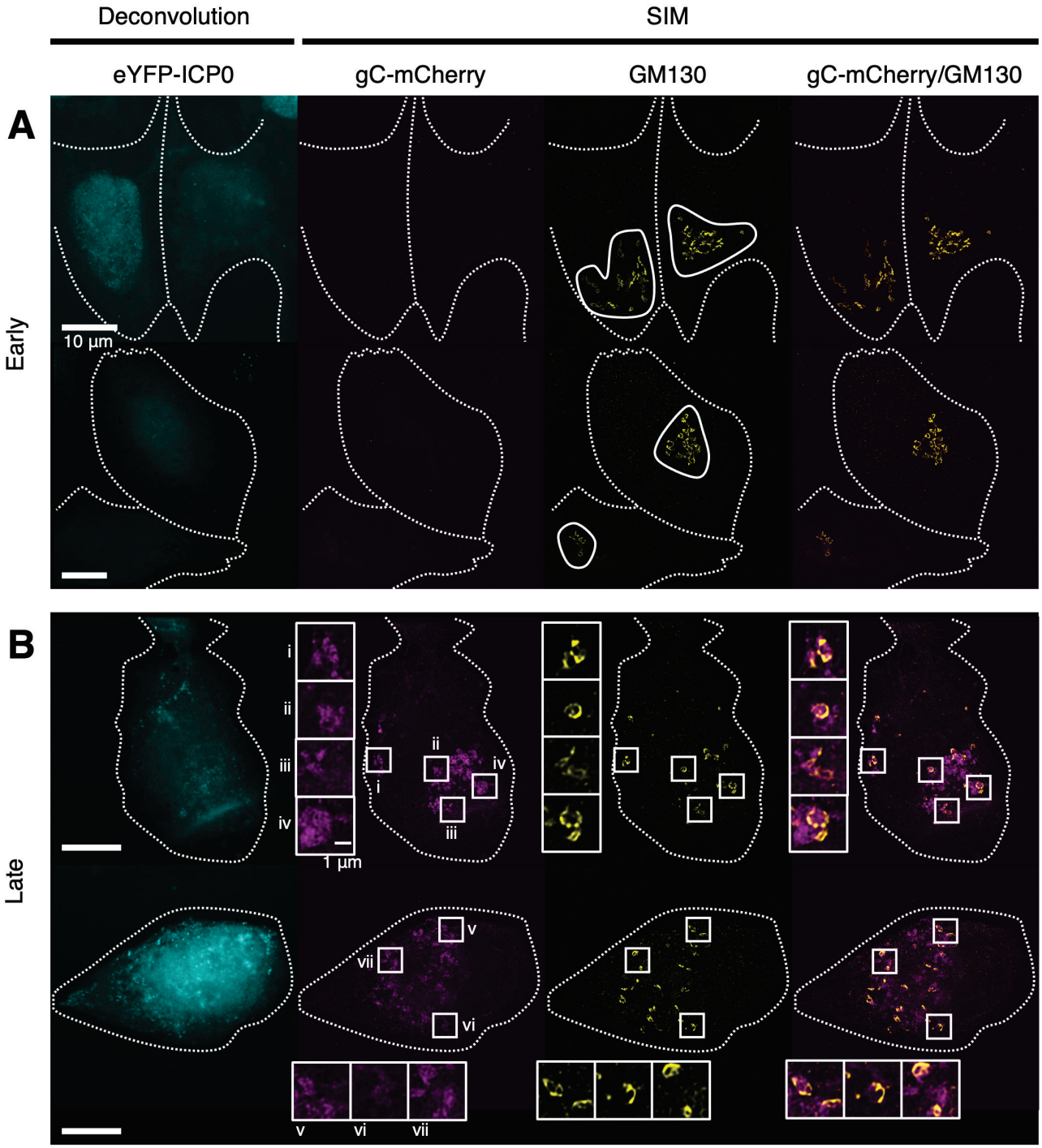

854 **Fig. 6. Fragmentation and dispersal of *cis*-Golgi membranes during HSV-1 infection.** U2OS cells
855 infected (MOI 3) with timestamp HSV-1 were fixed at 6 hpi and imaged by SIM and deconvolution
856 microscopy. GM130 immunolabelling was used to identify *cis*-Golgi membranes [107]. Dotted outlines
857 denote the cell boundaries. (**A**) Cells at early stages of infection were identified by the presence of
858 eYFP-ICP0 signal using deconvolution microscopy and by the absence of high gC-mCherry signal using
859 SIM. GM130^{+} membranes, which appeared clustered at early stages of infection, are outlined. (**B**) Cells

860 at late stages of infection were identified by the presence of high gC-mCherry signal. GM130^{+}
861 membranes were dispersed and fragmented in these cells. Boxes (i–vii) and corresponding insets
862 showing adjacent localization of GM130 and gC-mCherry.

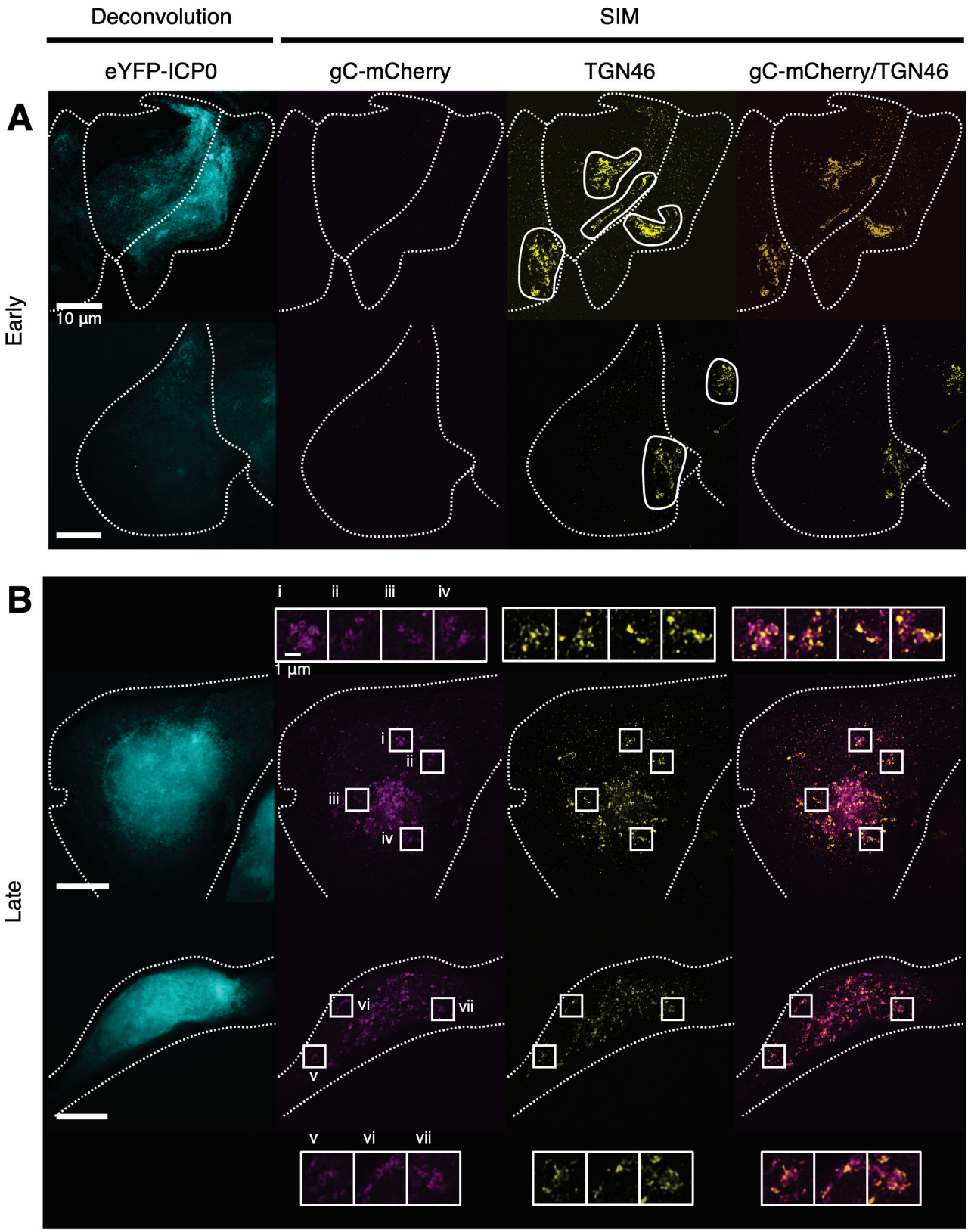

863 **Fig. 7. Fragmentation and dispersal of *trans*-Golgi membranes during HSV-1 infection.** U2OS
864 cells infected (MOI 3) with timestamp HSV-1 were fixed 6 hpi and imaged by SIM and deconvolution
865 microscopy. TGN46 immunolabelling was used to identify *trans*-Golgi network membranes [108].

866 Dotted outlines denote the cell boundaries. (**A**) Cells at early stages of infection were identified by the
867 presence of eYFP-ICP0 signal using deconvolution microscopy and by the absence of high gC-mCherry
868 signal using SIM. TGN46^{+} membranes, which appeared both clustered and dispersed at early stages
869 of infection, are outlined. (**B**) Cells at late stages of infection were identified by the presence of high gC-
870 mCherry signal using SIM and TGN46^{+} membranes were widely dispersed in these cells. Boxes (i–vii)
871 and corresponding insets indicate sites of colocalization and adjacent signal between TGN46 and gC-
872 mCherry.

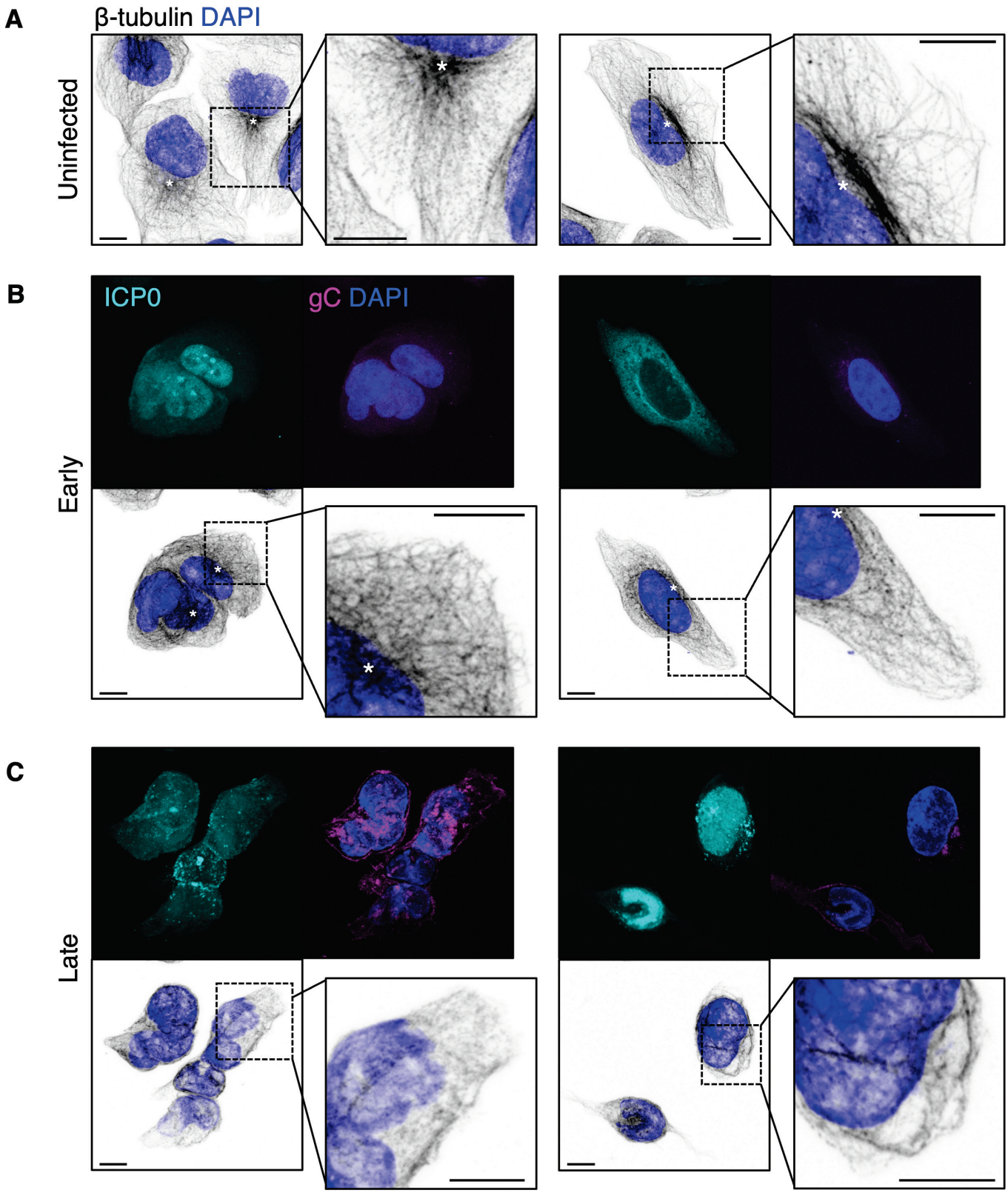

873 **Fig. 8. Remodelling of microtubules during HSV-1 infection.** U2OS cells infected with timestamp
874 HSV-1 were fixed at indicated times and imaged by confocal microscopy. β-tubulin immunolabelling
875 was used to identify microtubules. Scale bars = 10 μm. Putative microtubule organising centres

876 (MTOCs) are indicated with asterisks (*). (**A**) Uninfected cells exhibited an outspread microtubule
877 network with long filaments, largely radiating from a putative MTOC. (**B**) The microtubule network was
878 closely packed in cells at early stages of infection (6 hpi). (**C**) In cells at late stages of infection (16 hpi),
879 fewer long filaments were observed, the cells lacked noticeable MTOCs, and the network became very
880 closely packed.
881

882 **References**

883 1. Nicoll MP, Proença JT, Efstathiou S. The molecular basis of herpes simplex virus latency. FEMS
884 Microbiol Rev. 2012;36: 684–705. doi:10.1111/j.1574-6976.2011.00320.x

885 2. Owen D, Crump C, Graham S. Tegument Assembly and Secondary Envelopment of
886 Alphaherpesviruses. Viruses. 2015;7: 5084–5114. doi:10.3390/v7092861

887 3. Ahmad I, Wilson DW. HSV-1 Cytoplasmic Envelopment and Egress. Int J Mol Sci. 2020;21:
888 5969. doi:10.3390/ijms21175969

889 4. Mettenleiter TC. Herpesvirus Assembly and Egress. J Virol. 2002;76: 1537–1547.
890 doi:10.1128/JVI.76.4.1537-1547.2002

891 5. Johnson DC, Baines JD. Herpesviruses remodel host membranes for virus egress. Nat Rev
892 Microbiol. 2011;9: 382–394. doi:10.1038/nrmicro2559

893 6. Crump C. Virus Assembly and Egress of HSV. In: Kawaguchi Y, Mori Y, Kimura H, editors.
894 Human Herpesviruses. Singapore: Springer Singapore; 2018. pp. 23–44. doi:10.1007/978-981-
895 10-7230-7_2

896 7. Brown JC, Newcomb WW. Herpesvirus capsid assembly: insights from structural analysis. Curr
897 Opin Virol. 2011;1: 142–149. doi:10.1016/j.coviro.2011.06.003

898 8. Bigalke JM, Heldwein EE. Structural basis of membrane budding by the nuclear egress complex
899 of herpesviruses. EMBO J. 2015;34: 2921–2936. doi:10.15252/embj.201592359

900 9. Bigalke JM, Heldwein EE. Nuclear Exodus: Herpesviruses Lead the Way. Annu Rev Virol.
901 2016;3: 387–409. doi:10.1146/annurev-virology-110615-042215

902 10. Zeev-Ben-Mordehai T, Weberruß M, Lorenz M, Cheleski J, Hellberg T, Whittle C, et al. Crystal
903 Structure of the Herpesvirus Nuclear Egress Complex Provides Insights into Inner Nuclear
904 Membrane Remodeling. Cell Rep. 2015;13: 2645–2652. doi:10.1016/j.celrep.2015.11.008

905 11. Bigalke JM, Heldwein EE. The Great (Nuclear) Escape: New Insights into the Role of the Nuclear
906 Egress Complex of Herpesviruses. J Virol. 2015;89: 9150–9153. doi:10.1128/JVI.02530-14

907 12. Hernández Durán A, Greco TM, Vollmer B, Cristea IM, Grünewald K, Topf M. Protein
908 interactions and consensus clustering analysis uncover insights into herpesvirus virion structure
909 and function relationships. PLoS Biol. 2019;17: e3000316. doi:10.1371/journal.pbio.3000316

910 13. Hollinshead M, Johns HL, Sayers CL, Gonzalez-Lopez C, Smith GL, Elliott G. Endocytic tubules
911 regulated by Rab GTPases 5 and 11 are used for envelopment of herpes simplex virus. EMBO
912 J. 2012;31: 4204–4220. doi:10.1038/emboj.2012.262

913 14. Kotsakis A, Pomeranz LE, Blouin A, Blaho JA. Microtubule Reorganization during Herpes
914 Simplex Virus Type 1 Infection Facilitates the Nuclear Localization of VP22, a Major Virion
915 Tegument Protein. J Virol. 2001;75: 8697–8711. doi:10.1128/JVI.75.18.8697-8711.2001

916 15. Kim JA, Kim JC, Min JS, Kang I, Oh J, Ahn JK. HSV-1 ICP27 induces apoptosis by promoting
917 Bax translocation to mitochondria through interacting with 14-3-3θ. BMB Rep. 2017;50: 257–
918 262. doi:10.5483/BMBRep.2017.50.5.023

919 16. Scherer KM, Manton JD, Soh TK, Mascheroni L, Connor V, Crump CM, et al. A fluorescent
920 reporter system enables spatiotemporal analysis of host cell modification during herpes simplex
921 virus-1 replication. J Biol Chem. 2021;296: 100236. doi:10.1074/jbc.RA120.016571

922 17. Martin C, Leyton L, Hott M, Arancibia Y, Spichiger C, McNiven MA, et al. Herpes Simplex Virus
923 Type 1 Neuronal Infection Perturbs Golgi Apparatus Integrity through Activation of Src Tyrosine
924 Kinase and Dyn-2 GTPase. Front Cell Infect Microbiol. 2017;7: 371.
925 doi:10.3389/fcimb.2017.00371

926 18. Maeda F, Arii J, Hirohata Y, Maruzuru Y, Koyanagi N, Kato A, et al. Herpes Simplex Virus 1
927 UL34 Protein Regulates the Global Architecture of the Endoplasmic Reticulum in Infected Cells.
928 J Virol. 2017;91: e00271-17. doi:10.1128/JVI.00271-17

929 19. Liu X, Hajnóczky G. Altered fusion dynamics underlie unique morphological changes in
930 mitochondria during hypoxia–reoxygenation stress. Cell Death Differ. 2011;18: 1561–1572.
931 doi:10.1038/cdd.2011.13

932 20. Li J, Huang Q, Long X, Guo X, Sun X, Jin X, et al. Mitochondrial elongation-mediated glucose
933 metabolism reprogramming is essential for tumour cell survival during energy stress. Oncogene.
934 2017;36: 4901–4912. doi:10.1038/onc.2017.98

935 21. Li Y, Boehning DF, Qian T, Popov VL, Weinman SA. Hepatitis C virus core protein increases
936 mitochondrial ROS production by stimulation of Ca2+ uniporter activity. FASEB J. 2007;21:
937 2474–2485. doi:10.1096/fj.06-7345com

938 22. Muraro SP, De Souza GF, Gallo SW, Da Silva BK, De Oliveira SD, Vinolo MAR, et al.
939 Respiratory Syncytial Virus induces the classical ROS-dependent NETosis through PAD-4 and
940 necroptosis pathways activation. Sci Rep. 2018;8: 14166. doi:10.1038/s41598-018-32576-y

941 23. Lassoued S, Ben Ameur R, Ayadi W, Gargouri B, Ben Mansour R, Attia H. Epstein-Barr virus
942 induces an oxidative stress during the early stages of infection in B lymphocytes, epithelial, and
943 lymphoblastoid cell lines. Mol Cell Biochem. 2008;313: 179–186. doi:10.1007/s11010-008-9755-
944 z

945 24. Youle RJ, van der Bliek AM. Mitochondrial Fission, Fusion, and Stress. Science. 2012;337:
946 1062–1065. doi:10.1126/science.1219855

947 25. Pasdeloup D, Labetoulle M, Rixon FJ. Differing Effects of Herpes Simplex Virus 1 and
948 Pseudorabies Virus Infections on Centrosomal Function. J Virol. 2013;87: 7102–7112.
949 doi:10.1128/JVI.00764-13

950 26. Ayache J, Beaunier L, Boumendil J, Ehret G, Laub D. Artifacts in Transmission Electron
951 Microscopy. Sample Preparation Handbook for Transmission Electron Microscopy. New York,
952 NY: Springer New York; 2010. pp. 125–170. doi:10.1007/978-0-387-98182-6_6

953 27. Schnell U, Dijk F, Sjollema KA, Giepmans BNG. Immunolabeling artifacts and the need for live-
954 cell imaging. Nat Methods. 2012;9: 152–158. doi:10.1038/nmeth.1855

955 28. Büttner M, Lagerholm CB, Waithe D, Galiani S, Schliebs W, Erdmann R, et al. Challenges of
956 Using Expansion Microscopy for Super-resolved Imaging of Cellular Organelles.
957 ChemBioChem. 2021;22: 686–693. doi:10.1002/cbic.202000571

958 29. Harkiolaki M, Darrow MC, Spink MC, Kosior E, Dent K, Duke E. Cryo-soft X-ray tomography:
959 using soft X-rays to explore the ultrastructure of whole cells. Ubbink M, Perrakis A, editors.
960 Emerg Top Life Sci. 2018;2: 81–92. doi:10.1042/ETLS20170086

961 30. Lewis RA. Medical phase contrast x-ray imaging: current status and future prospects. Phys Med
962 Biol. 2004;49: 3573–3583. doi:10.1088/0031-9155/49/16/005

963 31. Garman EF. Developments in X-ray Crystallographic Structure Determination of Biological
964 Macromolecules. Science. 2014;343: 1102–1108. doi:10.1126/science.1247829

965 32. Kounatidis I, Stanifer ML, Phillips MA, Paul-Gilloteaux P, Heiligenstein X, Wang H, et al. 3D
966 Correlative Cryo-Structured Illumination Fluorescence and Soft X-ray Microscopy Elucidates
967 Reovirus Intracellular Release Pathway. Cell. 2020;182: 515-530.e17.
968 doi:10.1016/j.cell.2020.05.051

969 33. Okolo CA, Kounatidis I, Groen J, Nahas KL, Balint S, Fish TM, et al. Sample preparation
970 strategies for efficient correlation of 3D SIM and soft X-ray tomography data at cryogenic
971 temperatures. Nat Protoc. 2021;16: 2851–2885. doi:10.1038/s41596-021-00522-4

972 34. Roos WH, Radtke K, Kniesmeijer E, Geertsema H, Sodeik B, Wuite GJL. Scaffold expulsion and
973 genome packaging trigger stabilization of herpes simplex virus capsids. Proc Natl Acad Sci U S
974 A. 2009;106: 9673–9678. doi:10.1073/pnas.0901514106

975 35. Lau S-Y, Crump C. HSV-1 gM and the gK/pUL20 Complex Are Important for the Localization of
976 gD and gH/L to Viral Assembly Sites. Viruses. 2015;7: 915–938. doi:10.3390/v7030915

977 36. Gao J, Finnen RL, Sherry MR, Le Sage V, Banfield BW. Differentiating the Roles of UL16, UL21,
978 and Us3 in the Nuclear Egress of Herpes Simplex Virus Capsids. J Virol. 2020;94: 00738–20.
979 doi:10.1128/JVI.00738-20

980 37. Laine RF, Albecka A, van de Linde S, Rees EJ, Crump CM, Kaminski CF. Structural analysis of
981 herpes simplex virus by optical super-resolution imaging. Nat Commun. 2015;6: 5980.
982 doi:10.1038/ncomms6980

983 38. Yuan S, Wang J, Zhu D, Wang N, Gao Q, Chen W, et al. Cryo-EM structure of a herpesvirus
984 capsid at 3.1 Å. Science. 2018;360: eaao7283. doi:10.1126/science.aao7283

985 39. Chichón FJ, Rodríguez MJ, Pereiro E, Chiappi M, Perdiguero B, Guttmann P, et al. Cryo X-ray
986 nano-tomography of vaccinia virus infected cells. J Struct Biol. 2012;177: 202–211.
987 doi:10.1016/j.jsb.2011.12.001

988 40. Myllys M, Ruokolainen V, Aho V, Smith EA, Hakanen S, Peri P, et al. Herpes simplex virus 1
989 induces egress channels through marginalized host chromatin. Sci Rep. 2016;6: 28844.
990 doi:10.1038/srep28844

991 41. von Hofsten O, Bertilson M, Reinspach J, Holmberg A, Hertz HM, Vogt U. Sub-25-nm laboratory
992 x-ray microscopy using a compound Fresnel zone plate. Opt Lett. 2009;34: 2631.
993 doi:10.1364/OL.34.002631

994 42. Mastronarde DN, Held SR. Automated tilt series alignment and tomographic reconstruction in
995 IMOD. J Struct Biol. 2017;197: 102–113. doi:10.1016/j.jsb.2016.07.011

996 43. Skepper JN, Whiteley A, Browne H, Minson A. Herpes Simplex Virus Nucleocapsids Mature to
997 Progeny Virions by an Envelopment → Deenvelopment → Reenvelopment Pathway. J Virol.
998 2001;75: 5697–5702. doi:10.1128/JVI.75.12.5697-5702.2001

999 44. Leuzinger H, Ziegler U, Schraner EM, Fraefel C, Glauser DL, Heid I, et al. Herpes Simplex Virus
1000 1 Envelopment Follows Two Diverse Pathways. J Virol. 2005;79: 13047–13059.
1001 doi:10.1128/JVI.79.20.13047-13059.2005

1002 45. Hagen C, Dent KC, Zeev-Ben-Mordehai T, Grange M, Bosse JB, Whittle C, et al. Structural
1003 Basis of Vesicle Formation at the Inner Nuclear Membrane. Cell. 2015;163: 1692–1701.
1004 doi:10.1016/j.cell.2015.11.029

1005 46. Baines JD, Wills E, Jacob RJ, Pennington J, Roizman B. Glycoprotein M of Herpes Simplex
1006 Virus 1 Is Incorporated into Virions during Budding at the Inner Nuclear Membrane. J Virol.
1007 2007;81: 800–812. doi:10.1128/JVI.01756-06

1008 47. Blondeau C, Pelchen-Matthews A, Mlcochova P, Marsh M, Milne RSB, Towers GJ. Tetherin
1009 Restricts Herpes Simplex Virus 1 and Is Antagonized by Glycoprotein M. J Virol. 2013;87:
1010 13124–13133. doi:10.1128/JVI.02250-13

1011 48. Zenner HL, Mauricio R, Banting G, Crump CM. Herpes simplex virus 1 counteracts tetherin
1012 restriction via its virion host shutoff activity. J Virol. 2013;87: 13115–13123.
1013 doi:10.1128/JVI.02167-13

1014 49. Johnson DC, Webb M, Wisner TW, Brunetti C. Herpes Simplex Virus gE/gI Sorts Nascent
1015 Virions to Epithelial Cell Junctions, Promoting Virus Spread. J Virol. 2001;75: 821–833.
1016 doi:10.1128/JVI.75.2.821-833.2001

1017 50. Vijayakrishnan S, McElwee M, Loney C, Rixon F, Bhella D. In situ structure of virus capsids
1018 within cell nuclei by correlative light and cryo-electron tomography. Sci Rep. 2020;10: 17596.
1019 doi:10.1038/s41598-020-74104-x

1020 51. Grünewald K, Desai P, Winkler DC, Heymann JB, Belnap DM, Baumeister W, et al. Three-
1021 Dimensional Structure of Herpes Simplex Virus from Cryo-Electron Tomography. Science.
1022 2003;302: 1396–1398. doi:10.1126/science.1090284

1023 52. Drayman N, Patel P, Vistain L, Tay S. HSV-1 single-cell analysis reveals the activation of anti-
1024 viral and developmental programs in distinct sub-populations. eLife. 2019;8: e46339.
1025 doi:10.7554/eLife.46339

1026 53. Simpson-Holley M, Colgrove RC, Nalepa G, Harper JW, Knipe DM. Identification and Functional
1027 Evaluation of Cellular and Viral Factors Involved in the Alteration of Nuclear Architecture during
1028 Herpes Simplex Virus 1 Infection. J Virol. 2005;79: 12840–12851. doi:10.1128/JVI.79.20.12840-
1029 12851.2005

1030 54. Deng Z, Kim ET, Vladimirova O, Dheekollu J, Wang Z, Newhart A, et al. HSV-1 Remodels Host
1031 Telomeres to Facilitate Viral Replication. Cell Rep. 2014;9: 2263–2278.
1032 doi:10.1016/j.celrep.2014.11.019

1033 55. Cai W, Schaffer PA. Herpes simplex virus type 1 ICP0 regulates expression of immediate-early,
1034 early, and late genes in productively infected cells. J Virol. 1992;66: 2904–2915.
1035 doi:10.1128/jvi.66.5.2904-2915.1992

1036 56. Deschamps T, Kalamvoki M. Impaired STING Pathway in Human Osteosarcoma U2OS Cells
1037 Contributes to the Growth of ICP0-Null Mutant Herpes Simplex Virus. J Virol. 2017;91: e00006-
1038 17. doi:10.1128/JVI.00006-17

1039 57. Visalli RJ, Brandt CR. The HSV-1 UL45 18 kDa gene product is a true late protein and a
1040 component of the virion. Virus Res. 1993;29: 167–178. doi:10.1016/0168-1702(93)90057-T

1041 58. Loret S, Guay G, Lippé R. Comprehensive Characterization of Extracellular Herpes Simplex
1042 Virus Type 1 Virions. J Virol. 2008;82: 8605–8618. doi:10.1128/JVI.00904-08

1043 59. Müller WG, Bernard Heymann J, Nagashima K, Guttmann P, Werner S, Rehbein S, et al.
1044 Towards an atlas of mammalian cell ultrastructure by cryo soft X-ray tomography. J Struct Biol.
1045 2012;177: 179–192. doi:10.1016/j.jsb.2011.11.025

1046 60. Nahas KL, Fernandes JF, Vyas N, Crump C, Graham S, Harkiolaki M. Contour, a semi-
1047 automated segmentation and quantitation tool for cryo-soft-X-ray tomography. Biol Imaging.
1048 2022;2: e3. doi:10.1017/S2633903X22000046

1049 61. Sun MG, Williams J, Munoz-Pinedo C, Perkins GA, Brown JM, Ellisman MH, et al. Correlated
1050 three-dimensional light and electron microscopy reveals transformation of mitochondria during
1051 apoptosis. Nat Cell Biol. 2007;9: 1057–1065. doi:10.1038/ncb1630

1052 62. Miyazono Y, Hirashima S, Ishihara N, Kusukawa J, Nakamura K, Ohta K. Uncoupled
1053 mitochondria quickly shorten along their long axis to form indented spheroids, instead of rings,
1054 in a fission-independent manner. Sci Rep. 2018;8: 350. doi:10.1038/s41598-017-18582-6

1055 63. Eustaquio T, Wang C, Dugard CK, George NI, Liu F, Slikker W, et al. Electron microscopy
1056 techniques employed to explore mitochondrial defects in the developing rat brain following
1057 ketamine treatment. Exp Cell Res. 2018;373: 164–170. doi:10.1016/j.yexcr.2018.10.009

1058 64. Avitabile E, Di Gaeta S, Torrisi MR, Ward PL, Roizman B, Campadelli-Fiume G. Redistribution
1059 of microtubules and Golgi apparatus in herpes simplex virus-infected cells and their role in viral
1060 exocytosis. J Virol. 1995;69: 7472–7482. doi:10.1128/jvi.69.12.7472-7482.1995

1061 65. Campadelli G, Brandimarti R, Di Lazzaro C, Ward PL, Roizman B, Torrisi MR. Fragmentation
1062 and dispersal of Golgi proteins and redistribution of glycoproteins and glycolipids processed
1063 through the Golgi apparatus after infection with herpes simplex virus 1. Proc Natl Acad Sci U S
1064 A. 1993;90: 2798–2802. doi:10.1073/pnas.90.7.2798

1065 66. Melkov A, Abdu U. Regulation of long-distance transport of mitochondria along microtubules.
1066 Cell Mol Life Sci. 2018;75: 163–176. doi:10.1007/s00018-017-2590-1

1067 67. Jin Y, Ren Z, Tan Y, Zhao P, Wu J. Motility Plays an Important Role in the Lifetime of Mammalian
1068 Lipid Droplets. Int J Mol Sci. 2021;22: 3802. doi:10.3390/ijms22083802

1069 68. Fourriere L, Jimenez AJ, Perez F, Boncompain G. The role of microtubules in secretory protein
1070 transport. J Cell Sci. 2020;133: jcs237016. doi:10.1242/jcs.237016

1071 69. Lee GE, Murray JW, Wolkoff AW, Wilson DW. Reconstitution of Herpes Simplex Virus
1072 Microtubule-Dependent Trafficking In Vitro. J Virol. 2006;80: 4264–4275.
1073 doi:10.1128/JVI.80.9.4264-4275.2006

1074 70. Mikhaylova M, Cloin BMC, Finan K, van den Berg R, Teeuw J, Kijanka MM, et al. Resolving
1075 bundled microtubules using anti-tubulin nanobodies. Nat Commun. 2015;6: 7933.
1076 doi:10.1038/ncomms8933

1077 71. Carzaniga R, Domart M-C, Collinson LM, Duke E. Cryo-soft X-ray tomography: a journey into
1078 the world of the native-state cell. Protoplasma. 2014;251: 449–458. doi:10.1007/s00709-013-
1079 0583-y

1080 72. Yücelen E, Lazić I, Bosch EGT. Phase contrast scanning transmission electron microscopy
1081 imaging of light and heavy atoms at the limit of contrast and resolution. Sci Rep. 2018;8: 2676.
1082 doi:10.1038/s41598-018-20377-2

1083 73. Turk M, Baumeister W. The promise and the challenges of cryo-electron tomography. FEBS
1084 Lett. 2020;594: 3243–3261. doi:10.1002/1873-3468.13948

1085 74. Merk A, Bartesaghi A, Banerjee S, Falconieri V, Rao P, Davis MI, et al. Breaking Cryo-EM
1086 Resolution Barriers to Facilitate Drug Discovery. Cell. 2016;165: 1698–1707.
1087 doi:10.1016/j.cell.2016.05.040

1088 75. Erdmann PS, Hou Z, Klumpe S, Khavnekar S, Beck F, Wilfling F, et al. In situ cryo-electron
1089 tomography reveals gradient organization of ribosome biogenesis in intact nucleoli. Nat
1090 Commun. 2021;12: 5364. doi:10.1038/s41467-021-25413-w

1091 76. Albert S, Schaffer M, Beck F, Mosalaganti S, Asano S, Thomas HF, et al. Proteasomes tether
1092 to two distinct sites at the nuclear pore complex. Proc Natl Acad Sci U S A. 2017;114: 13726–
1093 13731. doi:10.1073/pnas.1716305114

1094 77. Risco C, Sanmartín-Conesa E, Tzeng W, Frey T, Seybold V, de Groot R. Specific, Sensitive,
1095 High-Resolution Detection of Protein Molecules in Eukaryotic Cells Using Metal-Tagging
1096 Transmission Electron Microscopy. Structure. 2012;20: 759–766.

1097 78. Samrat SK, Ha BL, Zheng Y, Gu H. Characterization of Elements Regulating the Nuclear-to-
1098 Cytoplasmic Translocation of ICP0 in Late Herpes Simplex Virus 1 Infection. J Virol. 2018;92:
1099 e01673-17. doi:10.1128/JVI.01673-17

1100 79. Lopez P, Van Sant C, Roizman B. Requirements for the Nuclear-Cytoplasmic Translocation of
1101 Infected-Cell Protein 0 of Herpes Simplex Virus 1. J Virol. 2001;75: 3832–3840.
1102 doi:10.1128/JVI.75.8.3832-3840.2001

1103 80. Lengyel J, Strain AK, Perkins KD, Rice SA. ICP27-dependent resistance of herpes simplex virus
1104 type 1 to leptomycin B is associated with enhanced nuclear localization of ICP4 and ICP0.
1105 Virology. 2006;352: 368–379. doi:10.1016/j.virol.2006.04.044

1106 81. Cai M, Wang P, Wang Y, Chen T, Xu Z, Zou X, et al. Identification of the molecular determinants
1107 for nuclear import of PRV EP0. Biol Chem. 2019;400: 1385–1394. doi:10.1515/hsz-2019-0201

1108 82. Vyas N, Perry N, Okolo CA, Kounatidis I, Fish TM, Nahas KL, et al. Cryo-Structured Illumination
1109 Microscopic Data Collection from Cryogenically Preserved Cells. J Vis Exp. 2021; 62274.
1110 doi:10.3791/62274

1111 83. Monson EA, Crosse KM, Duan M, Chen W, O'Shea RD, Wakim LM, et al. Intracellular lipid
1112 droplet accumulation occurs early following viral infection and is required for an efficient
1113 interferon response. Nat Commun. 2021;12: 4303. doi:10.1038/s41467-021-24632-5

1114 84. Yu Y, Maguire TG, Alwine JC. Human Cytomegalovirus Infection Induces Adipocyte-Like
1115 Lipogenesis through Activation of Sterol Regulatory Element Binding Protein 1. J Virol. 2012;86:
1116 2942–2949. doi:10.1128/JVI.06467-11

1117 85. Seo J-Y, Cresswell P. Viperin regulates cellular lipid metabolism during human cytomegalovirus
1118 infection. PLoS Pathog. 2013;9: e1003497. doi:10.1371/journal.ppat.1003497

1119 86. Sukhorukov VM, Dikov D, Reichert AS, Meyer-Hermann M. Emergence of the mitochondrial
1120 reticulum from fission and fusion dynamics. PLoS Comput Biol. 2012;8: e1002745.
1121 doi:10.1371/journal.pcbi.1002745

1122 87. Bartolák-Suki E, Imsirovic J, Nishibori Y, Krishnan R, Suki B. Regulation of Mitochondrial
1123 Structure and Dynamics by the Cytoskeleton and Mechanical Factors. Int J Mol Sci. 2017;18:
1124 1812. doi:10.3390/ijms18081812

1125 88. Bowes T, Gupta RS. Novel mitochondrial extensions provide evidence for a link between
1126 microtubule-directed movement and mitochondrial fission. Biochem Biophys Res Commun.
1127 2008;376: 40–45. doi:10.1016/j.bbrc.2008.08.120

1128 89. Silva Ramos E, Larsson N-G, Mourier A. Bioenergetic roles of mitochondrial fusion. Biochim
1129 Biophys Acta BBA - Bioenerg. 2016;1857: 1277–1283. doi:10.1016/j.bbabio.2016.04.002

1130 90. Combs JA, Norton EB, Saifudeen ZR, Bentrup KHZ, Katakam PV, Morris CA, et al. Human
1131 Cytomegalovirus Alters Host Cell Mitochondrial Function during Acute Infection. J Virol. 2020;94:
1132 e01183-19. doi:10.1128/JVI.01183-19

1133 91. Chatel-Chaix L, Cortese M, Romero-Brey I, Bender S, Neufeldt CJ, Fischl W, et al. Dengue Virus
1134 Perturbs Mitochondrial Morphodynamics to Dampen Innate Immune Responses. Cell Host
1135 Microbe. 2016;20: 342–356. doi:10.1016/j.chom.2016.07.008

1136 92. Tanaka M, Sata T, Kawaguchi Y. The product of the Herpes simplex virus 1 UL7 gene interacts
1137 with a mitochondrial protein, adenine nucleotide translocator 2. Virol J. 2008;5: 125.
1138 doi:10.1186/1743-422X-5-125

1139 93. Derakhshan M, Willcocks MM, Salako MA, Kass GEN, Carter MJ. Human herpesvirus 1 protein
1140 US3 induces an inhibition of mitochondrial electron transport. J Gen Virol. 2006;87: 2155–2159.
1141 doi:10.1099/vir.0.81949-0

1142 94. Saffran HA, Pare JM, Corcoran JA, Weller SK, Smiley JR. Herpes simplex virus eliminates host
1143 mitochondrial DNA. EMBO Rep. 2007;8: 188–193. doi:10.1038/sj.embor.7400878

1144 95. Chadha P, Sarfo A, Zhang D, Abraham T, Carmichael J, Han J, et al. Domain Interaction Studies
1145 of Herpes Simplex Virus 1 Tegument Protein UL16 Reveal Its Interaction with Mitochondria. J
1146 Virol. 2017;91: e01995-16. doi:10.1128/JVI.01995-16

1147 96. McSharry BP, Jones CJ, Skinner JW, Kipling D, Wilkinson GWG. Human telomerase reverse
1148 transcriptase-immortalized MRC-5 and HCA2 human fibroblasts are fully permissive for human
1149 cytomegalovirus. J Gen Virol. 2001;82: 855–863. doi:10.1099/0022-1317-82-4-855

1150 97. Albecka A, Owen DJ, Ivanova L, Brun J, Liman R, Davies L, et al. Dual Function of the pUL7-
1151 pUL51 Tegument Protein Complex in Herpes Simplex Virus 1 Infection. J Virol. 2017;91:
1152 e02196-16. doi:10.1128/JVI.02196-16

1153 98. Kilmartin JV, Wright B, Milstein C. Rat monoclonal antitubulin antibodies derived by using a new
1154 nonsecreting rat cell line. J Cell Biol. 1982;93: 576–582. doi:10.1083/jcb.93.3.576

1155 99. Young LJ, Ströhl F, Kaminski CF. A Guide to Structured Illumination TIRF Microscopy at High
1156 Speed with Multiple Colors. J Vis Exp. 2016; 53988. doi:10.3791/53988

1157 100. Müller M, Mönkemöller V, Hennig S, Hübner W, Huser T. Open-source image reconstruction of
1158 super-resolution structured illumination microscopy data in ImageJ. Nat Commun. 2016;7:
1159 10980. doi:10.1038/ncomms10980

1160 101. Schindelin J, Arganda-Carreras I, Frise E, Kaynig V, Longair M, Pietzsch T, et al. Fiji: an open-
1161 source platform for biological-image analysis. Nat Methods. 2012;9: 676–682.
1162 doi:10.1038/nmeth.2019

1163 102. Kenny M, Schoen I. Violin SuperPlots: visualizing replicate heterogeneity in large data sets.
1164 Pollard TD, editor. Mol Biol Cell. 2021;32: 1333–1334. doi:10.1091/mbc.E21-03-0130

1165 103. Gómez-Rubio V. ggplot2 - Elegant Graphics for Data Analysis (2nd Edition). J Stat Softw.
1166 2017;77. doi:10.18637/jss.v077.b02

1167 104. Racine JS. RStudio: A Platform-Independent IDE for R and Sweave: Software Review. J Appl
1168 Econom. 2012;27: 167–172. doi:10.1002/jae.1278

1169 105. Lord SJ, Velle KB, Mullins RD, Fritz-Laylin LK. SuperPlots: Communicating reproducibility and
1170 variability in cell biology. J Cell Biol. 2020;219: e202001064. doi:10.1083/jcb.202001064

1171 106. Dai X, Zhou ZH. Structure of the herpes simplex virus 1 capsid with associated tegument protein
1172 complexes. Science. 2018;360: eaao7298. doi:10.1126/science.aao7298

1173 107. Zhang C-H, Wang Z-B, Quan S, Huang X, Tong J-S, Ma J-Y, et al. GM130, a cis-Golgi protein,
1174 regulates meiotic spindle assembly and asymmetric division in mouse oocyte. Cell Cycle.
1175 2011;10: 1861–1870. doi:10.4161/cc.10.11.15797

1176 108. Wang H, Sun H-Q, Zhu X, Zhang L, Albanesi J, Levine B, et al. GABARAPs regulate PI4P-
1177 dependent autophagosome:lysosome fusion. Proc Natl Acad Sci U S A. 2015;112: 7015–7020.
1178 doi:10.1073/pnas.1507263112

1179 109. Shafaq-Zadah M, Dransart E, Johannes L. Clathrin-independent endocytosis, retrograde
1180 trafficking, and cell polarity. Curr Opin Cell Biol. 2020;65: 112–121.
1181 doi:10.1016/j.ceb.2020.05.009

1182

1183

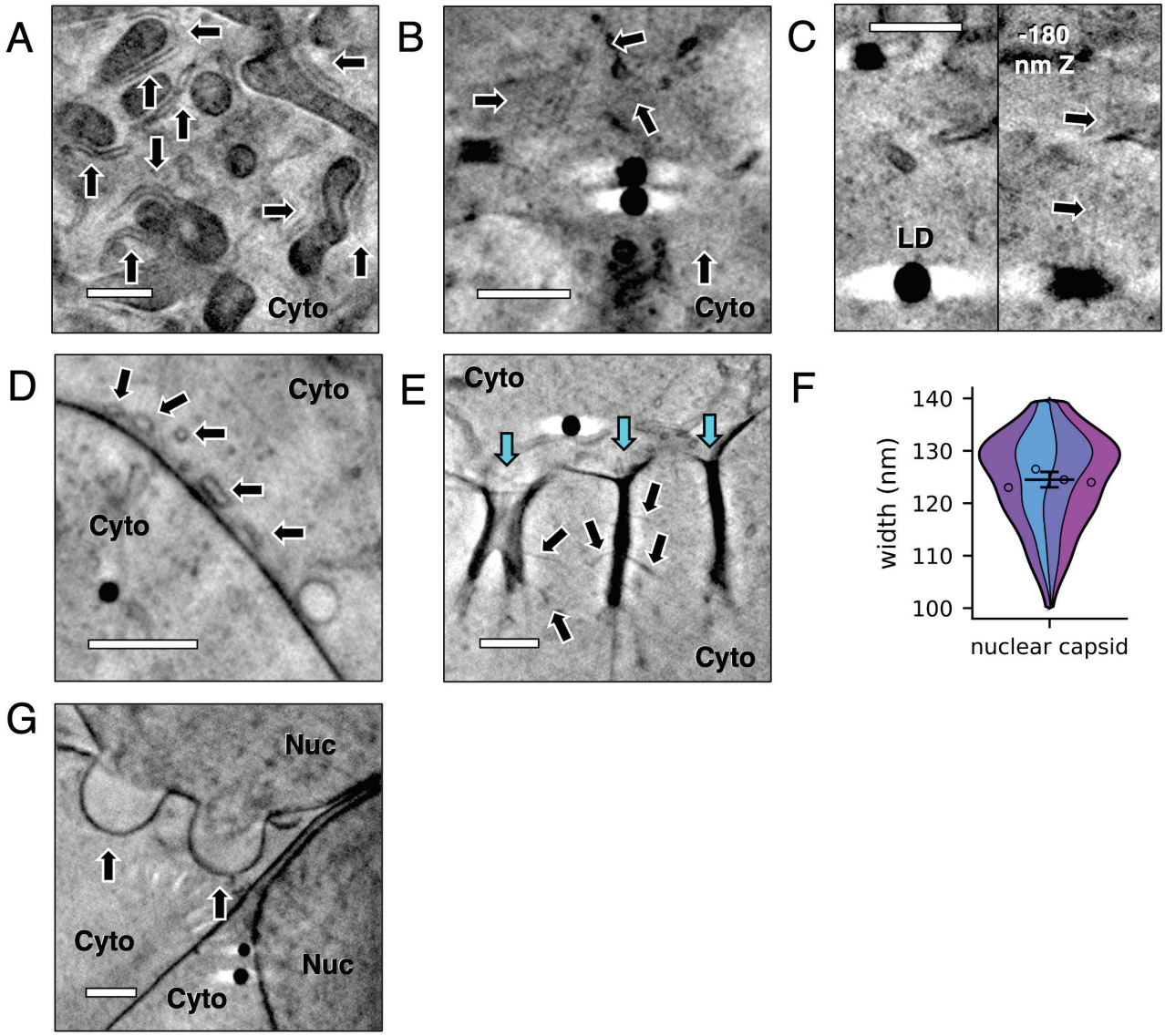

1184 **S1 Fig. High resolution structures visible with the 25 nm zone plate objective**. 139 CryoSXT
1185 tomograms were recorded from 107 cells using a 25 nm zone plate objective and several structures
1186 that were unrelated to HSV-1 infection were observed, including some that were not visible using the
1187 40 nm zone plate objective. (**A**) The endoplasmic reticulum (ER) forms a silhouette (arrows) around the
1188 mitochondria and the ER lumen is visible with the 25 nm zone plate. Cyto, cytoplasm. (**B**) Linear
1189 structures resembling cytoskeletal filaments are visible with the 25 nm zone plate (arrows). (**C**) A
1190 putative cytoskeletal filament (arrows) is in close apposition to a lipid droplet (LD) and may represent a
1191 physical interaction. (**D**) Small vesicles with widths of 150–300 nm in the peripheral cytoplasm are
1192 observed (arrows). (**E**) Large internalisations of the plasma membrane with depths of 1.6–2.2 μm (cyan
1193 arrows) and smaller side extensions (black arrows) are visible and may represent events of clathrin-
1194 independent bulk endocytosis [109]. (**F**) The width of nuclear capsids was remeasured after imaging

1195 with the 25 nm zone plate: 124.5 nm ± 0.96 nm SEM (n=80 from 4 tomograms; 8.55 nm SD). (**G**) Bulging
1196 of the nuclear envelope is observed (arrows). We initially observed these in HSV-1 infection and thought
1197 it may represent a virus-directed decrease in the integrity of the nuclear envelope, but we found multiple
1198 examples in uninfected cells suggesting that they are a characteristic of U2OS cells. Nuc, nucleus.
1199 Scale bars = 1μm.

1200

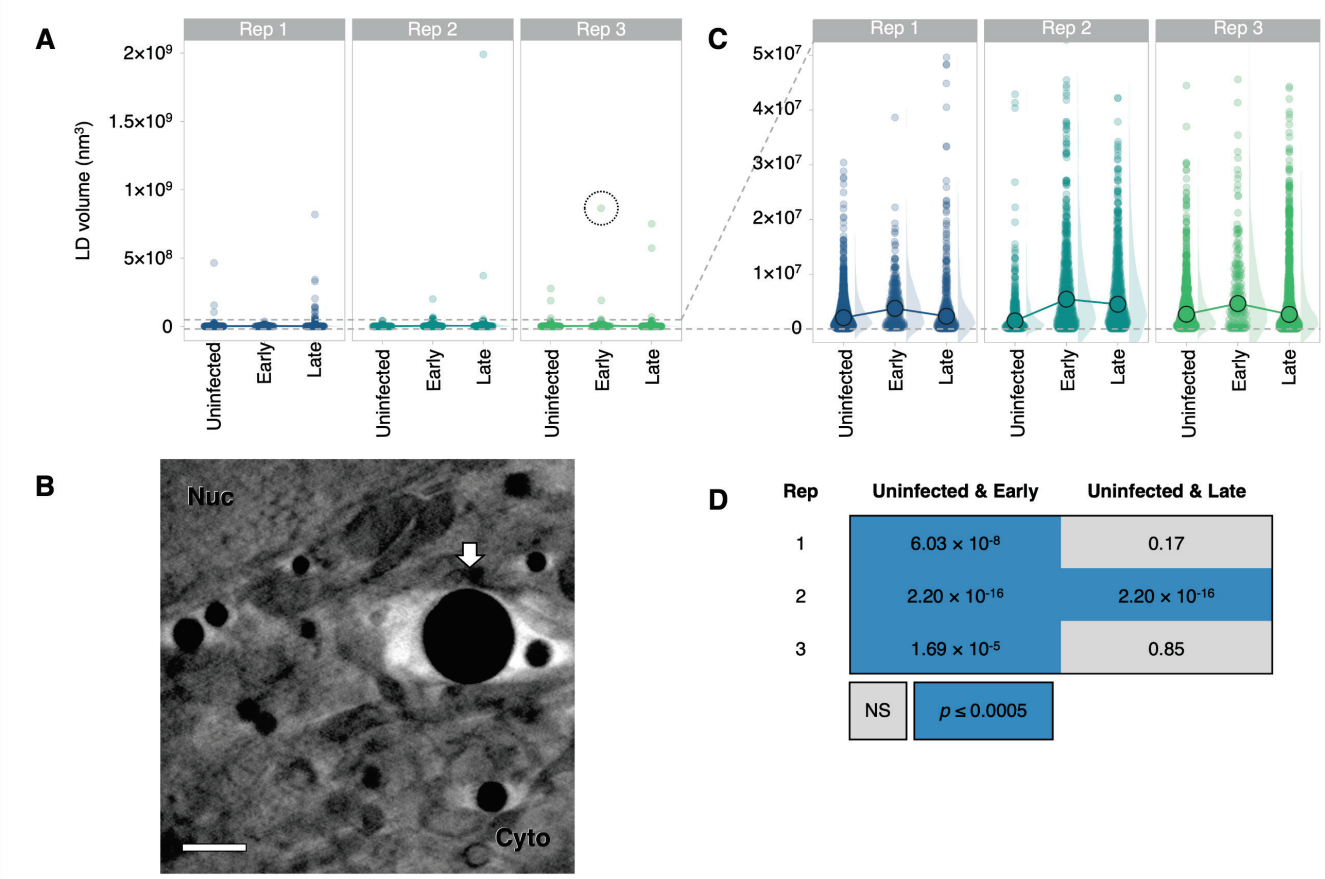

S2 Fig. Lipid droplets transiently increase in size during early stages of HSV-1 infection. 4845 lipid droplets across the three replicates were segmented using *Contour* [60] and their volumes were calculated. Scale bars = 1 μm. (**A**) A linear plot of lipid droplet volumes reveals a similar number of extremely large lipid droplets (> 5×10^7 nm^3) in U2OS cells. The circled lipid droplet is shown in (**B**). (**B**) A large lipid droplet observed in a U2OS cell at an early stage of infection. Scale bar = 1 μm. (**C**) A linear plot of lipid droplet volumes, truncated at 5×10^7 nm^3, reveals that in all conditions lipid droplet volumes were positively skewed rather than normally distributed. Median volumes are shown (large circles) because they are less affected by extreme values than mean volumes. The median lipid droplet volume was highest in cells at early stages of infection for all three replicates. (**D**) Given that the distributions were positively skewed, non-parametric Mann-Whitney *U* tests were carried out to determine significant differences at a 0.0005 *p*-value threshold. NS, no significant difference. In all three biological replicates the lipid droplets of cells at an early stage of infection are larger than in uninfected cells. The lipid droplets in cells at late stages of infection are not significantly larger than in uninfected cells for two of the three biological replicates, suggesting that a transient increase in lipid droplet volume accompanies HSV-1 infection of U2OS cells.

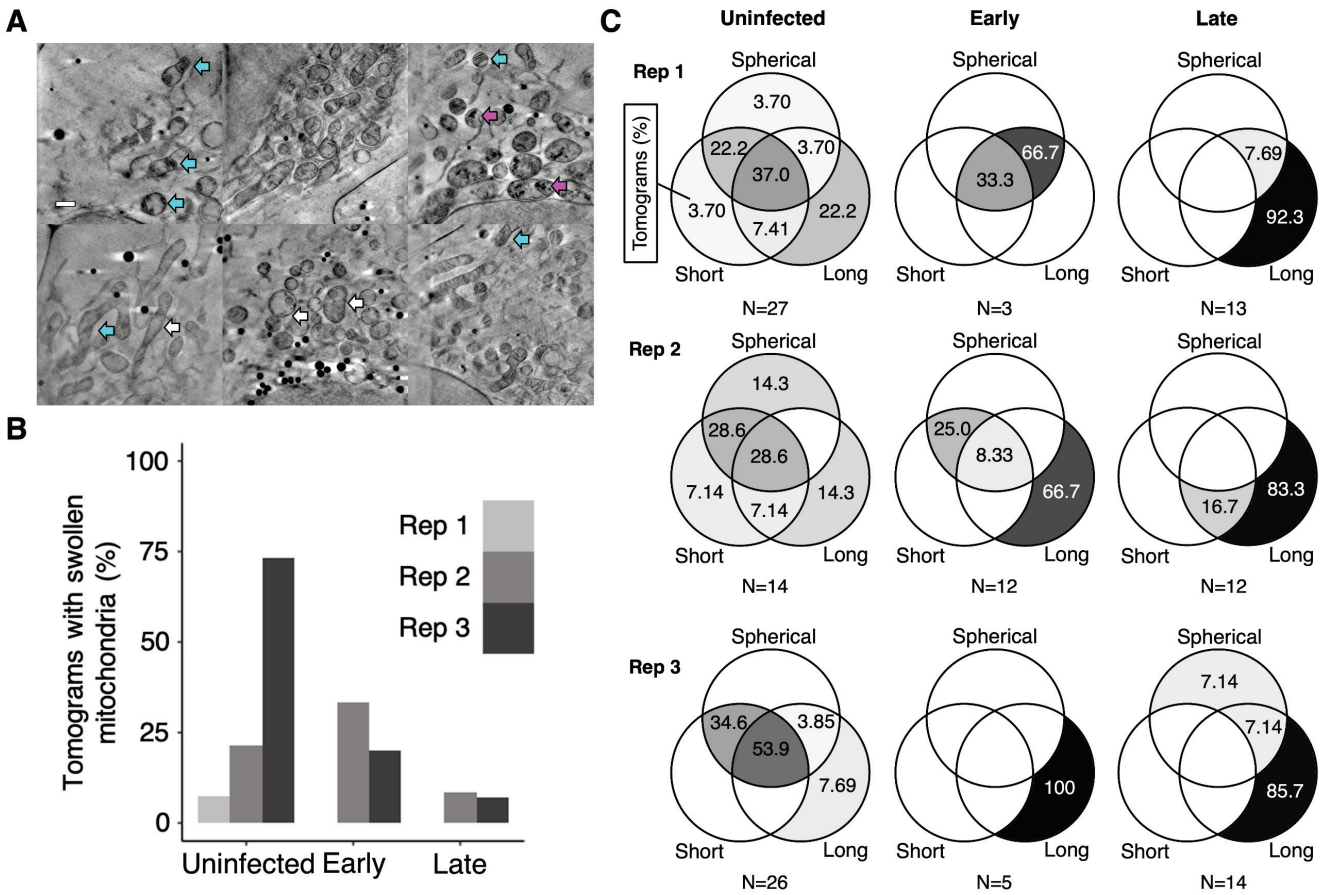

S3 Fig. The heterogenous morphology of mitochondria. Heterogenous mitochondrial morphologies are observed in cryoSXT tomograms collected from uninfected cells and cells at early and late stages of infection with timestamp HSV-1. Scale bars = 1 μm. (**A**) In some cases, mitochondria have light matrices with highly contrasting cristae (cyan arrows). This "swollen" phenotype has been reported to occur during cytochrome *c* release from porous mitochondria during apoptosis [61]. Dark matter is also observed in the matrix (magenta arrows) and may represent vesiculation. Small dark puncta are present in the matrix (white arrows) and could represent vesicles or short cristae. (**B**) The percentages of tomograms with swollen mitochondria for uninfected cells and cells at early- or late-stages of infection in three independent replicates. (**C**) The percentages of tomograms collected from uninfected cells and those at early- or late-stages on infection in each replicate that contain different combinations of mitochondrial morphologies.

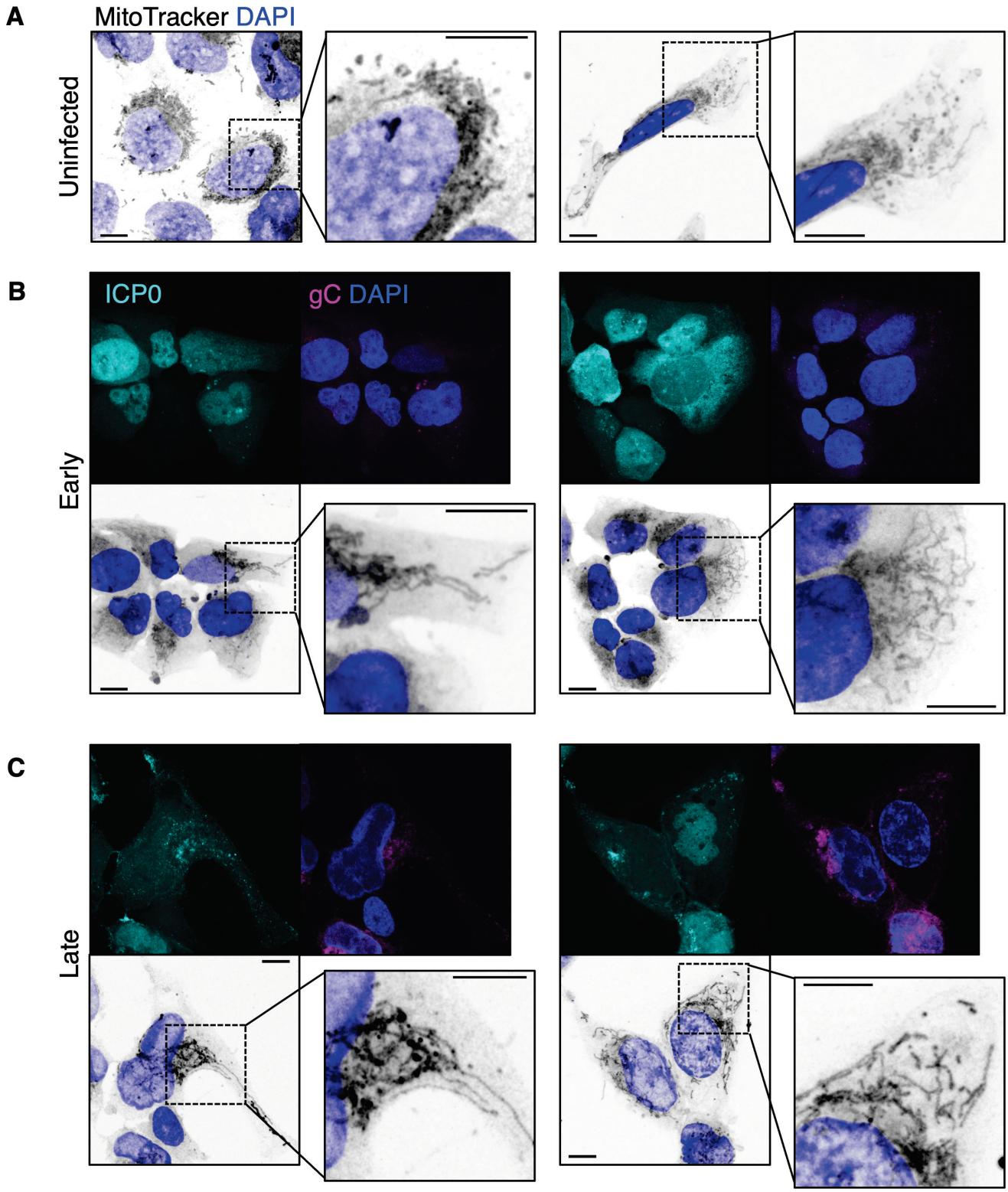

1227 **S4 Fig. Confocal imaging of mitochondrial morphology.** U2OS cells infected with timestamp HSV-
1228 1 (MOI 3) were fixed at indicated times and imaged by confocal microscopy. Mitochondria were stained
1229 with MitoTracker Deep Red FM. Scale bars = 10 μm. (**A**) Mitochondria in uninfected cells were

1230 morphologically heterogenous. (**B, C**) In cells at (**B**) early (6 hpi) and (**C**) late (16 hpi) stages of infection,
1231 a greater proportion of elongated mitochondria were observed.

1232 **S1 Video. Segmentation of vesicles and mitochondria in the cytoplasm of a cell at a late stage**
1233 **of infection.** CryoSXT data was collected from U2OS cells infected for 9 hours with the timestamp
1234 HSV-1 virus at an MOI of 1. Cryo-fluorescence microscopy revealed that this cell was at a late stage of
1235 infection. The mitochondria were segmented using *Contour* [60] and separate mitochondria are colour-
1236 coded in shades of orange, red, pink and purple. Cytoplasmic vesicles were segmented using
1237 *Segmentation Editor* in *ImageJ*. The vesicles were later differentiated and color-coded using *Contour*
1238 [60] and are displayed here in shades of blue and green. Field of view is 9.46×9.46 µm.

1239 **S2 Video. Segmentation of cytoplasmic vesicles reveals the effect of HSV-1 infection on vesicle**
1240 **concentration at juxtanuclear sites.** CryoSXT data was collected from uninfected U2OS cells and
1241 U2OS cells infected for 9 hours with the timestamp HSV-1 virus at an MOI of 1. Cytoplasmic vesicles
1242 were segmented using *Segmentation Editor* in *ImageJ*. The vesicles were later differentiated and
1243 colour-coded using *Contour* [60]. Fields of view are 9.46×9.46 µm.

1244 **S3 Video. Segmentation of mitochondria reveals the effect of HSV-1 infection on mitochondrial**
1245 **morphology.** CryoSXT data was collected from uninfected U2OS cells and U2OS cells infected for 9
1246 hours with the timestamp HSV-1 virus at an MOI of 1. Mitochondria were segmented and colour-coded
1247 using *Contour* [60] and appear elongated and branched in cells at late stages of infection. Fields of view
1248 are 9.46×9.46 µm.

1249